Title

Experimental Investigation of Gas Flow and Hydrate Formation Within the Hydrate Stability Zone

Journal

Journal of Geophysical Research: Solid Earth, 123(7)

ISSN

2169-9313

Authors

Meyer, Dylan W
Flemings, Peter B
DiCarlo, David
et al.

Publication Date

2018-07-01

DOI

10.1029/2018jb015748

Peer reviewed

Experimental Investigation of Gas Flow and Hydrate Formation Within the Hydrate Stability Zone

Dylan W. Meyer[1,2], Peter B. Flemings[1,2], David DiCarlo[3], Kehua You[1], Stephen C. Phillips[1], and Timothy J. Kneafsey[4]

[1] Institute for Geophysics, Jackson School of Geosciences, The University of Texas at Austin, Austin, TX, USA, [2] Department of Geological Sciences, Jackson School of Geosciences, The University of Texas at Austin, Austin, TX, USA, [3] Petroleum and Geosystems Engineering, The University of Texas at Austin, Austin, TX, USA, [4] Earth and Environmental Sciences, Lawrence Berkeley National Laboratory, Berkeley, CA, USA

Correspondence to: D. W. Meyer, meyerdw3@utexas.edu

Abstract

We form methane hydrate by injecting methane gas into a brine-saturated, coarse-grained sample under hydrate-stable thermodynamic conditions. Hydrate forms to a saturation of 11%, which is much lower than that predicted assuming three-phase (gas-hydrate-brine) thermodynamic equilibrium (67%). During hydrate formation, there are temporary flow blockages. We interpret that a hydrate skin forms a physical barrier at the gas-brine interface. The skin fails periodically when the pressure differential exceeds the skin strength. Once the skin is present, further hydrate formation is limited by the rate that methane can diffuse through the solid skin. This process produces distinct thermodynamic states on either side of the skin that allows gas to flow through the sample. This study illuminates how gas can be transported through the hydrate stability zone and thus provides a mechanism for the formation of concentrated hydrate deposits in sand reservoirs. It also illustrates that models that assume local equilibrium at the core-scale and larger may not capture the fundamental behaviors of these gas flow and hydrate formation processes.

Plain Language Summary

Methane hydrate is a crystalline solid composed of water and methane that forms at low temperature and high pressure. It is a major component of the carbon cycle and an enormous potential energy resource. It can be found in deep ocean sediments within thick, sandy layers above accumulations of methane gas. These hydrate deposits may form by the upward flow of buoyant methane gas from warm regions, where gas is stable, to cold regions, where hydrate is stable. We simulate this process experimentally by injecting gas into a cold, pressurized sand core. A significant amount of hydrate forms, and methane gas advances through the sand despite being in a region where it should solidify into hydrate. Our analysis of the X-ray images and the fluid volumes and pressures suggests that, during injection, a thin hydrate skin forms at the gas-brine interface. The hydrate skin separates the gas from the liquid and limits hydrate formation, allowing gas

to flow through the sand. This mechanism may form high concentrations of hydrates in sands in geologic systems.

1 Introduction

Gas hydrate is a crystalline compound composed of a low molecular weight gas, most commonly methane, encased in a water lattice (Kvenvolden & McMenamin, 1980). It is stable at low temperature, low salinity, and high pressure where the methane concentration is above the solubility limit (Sloan & Koh, 2007). As a result, hydrate primarily forms in marine sediments along continental margins and beneath permafrost (Boswell & Collett, 2011).

Approximately, 10% of natural hydrate occurs in coarse-grained material (Boswell & Collett, 2011), which have favorable production characteristics (Boswell & Collett, 2011; Moridis et al., 2009; Yamamoto et al., 2014). Some of these reservoirs consist of thick, dipping, sand layers, bounded by low permeability material, that contain gas hydrate above and free gas below the hydrate stability zone (Boswell, Collett, et al., 2012; Boswell et al., 2009; Crutchley et al., 2015; Tréhu et al., 2004). Hydrate exists in these sand layers far above the base of hydrate stability at saturations ranging between 60 and 90% (Collett et al., 2012). The processes responsible for the formation of these thick, high concentration, hydrate deposits far above the base of hydrate stability remain a conundrum.

Three mechanisms are proposed for the formation of high hydrate concentrations in sand reservoirs: (1) short-range diffusion of dissolved methane into a sand layer from surrounding fine-grained material, (2) long-range advection of dissolved methane upward into the gas hydrate stability zone (GHSZ) and associated short-range methane diffusion, and (3) long-range, buoyancy-driven advection of free methane gas into the GHSZ from below.

The first two mechanisms have been modeled (Cook & Malinverno, 2013; Nole et al., 2016; You & Flemings, 2017), with some field (Davie & Buffett, 2003; Malinverno & Goldberg, 2015; You & Flemings, 2017) and experimental (Priegnitz et al., 2013; Spangenberg et al., 2005) verification. In thick sands, short-range diffusion generates high hydrate concentrations at the boundaries of the sand, but low concentrations in the center (Rempel, 2011; You & Flemings, 2017). Long-range advection and diffusion of dissolved methane can result in significant saturations of hydrate but requires very long time scales due to the low methane solubility in water and small solubility gradient between the advecting and surrounding fluids (Davie & Buffett, 2003; Nole et al., 2016; Rempel & Buffett, 1997; Torres et al., 2004; Xu & Ruppel, 1999).

The advection of free methane gas into the GHSZ has also been modeled (Liu & Flemings, 2007; Torres et al., 2004; You, Kneafsey, et al., 2015) and studied in the field (Haeckel et al., 2004; Liu & Flemings, 2006; Tréhu et al.,

2004). In this mechanism, free methane gas below the GHSZ migrates upward, driven by buoyancy, and preferentially accumulates in high permeability, coarse-grained layers (England et al., 1987; Schowalter, 1979). The high capillary entry pressure of the fine-grained material above the sand restricts vertical gas transport (England et al., 1987; Schowalter, 1979). Instead, gas migrates updip into the GHSZ, forming hydrate (Liu & Flemings, 2006; Torres et al., 2004; Tréhu et al., 2004) and elevating the local pore fluid salinity (Hesse & Harrison, 1981; Torres et al., 2004; Ussler & Paull, 2001). With continual gas supply, hydrate forms until the local salinity is elevated to the three-phase concentration (Liu & Flemings, 2007; You, DiCarlo, et al., 2015), which occurs at the three-phase (gas, liquid, and hydrate) equilibrium hydrate saturation (S_{heq}). At three-phase equilibrium, hydrate formation is limited and gas migrates farther into the GHSZ (Liu & Flemings, 2007; Torres et al., 2004; You, DiCarlo, et al., 2015). This process produces an upward-propagating hydrate formation front with hydrate, gas, and water present at three-phase equilibrium conditions behind the front and brine at initial salinity present ahead of the front.

In this study, we performed experiments to elucidate the process of hydrate formation through gas injection. We injected methane gas into brine-saturated, coarse-grained samples under hydrate-stable conditions. Approximately 40% of the methane injected was converted into hydrate, resulting in bulk hydrate saturation within the affected volume of 11%, far below that predicted by bulk thermodynamic equilibrium (67%). We propose that a hydrate skin forms at the gas-brine interface that separates the gas and brine phases. The skin limits hydrate formation and forms local and distinct thermodynamic states on either side of the hydrate skin but does not significantly impede gas flow. This process provides a mechanism for gas transport through the hydrate stability zone. It also illustrates that models that assume local thermodynamic equilibrium at the core-scale and larger may not capture the fundamental physics of gas transport and hydrate formation in the hydrate stability zone.

2 Methods

2.1 Experimental Setup

We performed each experiment in a vertical pressure vessel consisting of steel endcaps and an X-ray transparent, aluminum cylinder surrounded by a cooling jacket (Figure 1), similar to other hydrate formation cells (Kneafsey et al., 2007; Seol & Kneafsey, 2009; You, Kneafsey, et al., 2015). We packed the sediment samples in a Viton® sleeve (17.8 cm length; 5.1 cm internal diameter; 0.25 cm wall thickness) that was sealed on each end with steel endcaps. The endcaps were fitted with stainless steel filters, to prevent sediment migration out of the sample.

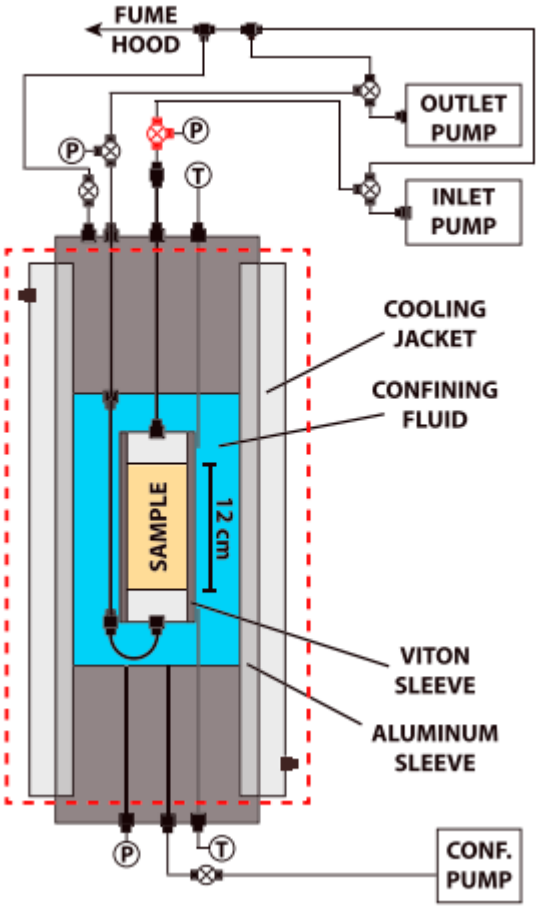

Figure 1

Diagram of the experimental apparatus. The sample (approx. 12 cm length and 5 cm diameter) was suspended within the confining cell. Two thermistors (*T*) recorded the confining temperature, three syringe pumps controlled the fluid flow, and three pressure transducers (*P*) tracked the pressure of the pore and confining fluids. The inlet valve that separated the gas and brine prior to the experiment is colored red. The red dashed line indicates the portion of the system that was in the hydrate stability zone.

We recorded 5-min moving averages of the pressure and temperature data and recorded the pump volume data every 5 min. We used three Teledyne ISCO syringe pumps (flow accuracy ±0.9 nL/hr; pump resolution = 31.7 nL) to separately control the downstream brine flow rate (outlet), upstream methane pressure (inlet), and confining pressure (Figure 1). We used three UNIK 5000 pressure transducers to monitor the confining (P_{conf}), methane (P_{in}), and brine (P_{out}) pressures (Figure 1). We recorded the confining fluid temperature using two thermistors located in the confining cell, near the top and bottom of the sample (Figure 1), and tracked the ambient temperature using a thermocouple near the inlet pump. We used these data to confirm that the confining and ambient temperatures were kept constant (±0.2°C) and to calculate temperature corrections for the gas pump volume. We did not directly measure the temperature inside the sample. However, the thermal diffusivity of saturated sands (α) is approximately 10^{-6} m^2 s^{-1} (Liu &

Flemings, 2007), which indicates a generic time scale for conduction ($\tau = r_{smpl}^2/\alpha$) across the sample radius (r_{smpl}) of approximately 0.18 hr. Since our experiments were run over the course of 85 hr, there was ample time for heat to dissipate by conduction. Thus, the confining thermistors provided a reasonable estimation of the internal sample temperature.

2.2 Sample Preparation

Each sample consisted primarily of medium (362-μm median grain size; 263-μm 10th percentile; 502-μm 90th percentile), uniform (1.48 uniformity coefficient; Lambe, 1969), silica sand from Sigma-Aldrich® (product no. 274739). We added 0.5 wt % smectite-rich clay from the Gulf of Mexico in the Eugene Island protraction area (Casey et al., 2013) to accelerate hydrate nucleation (Riestenberg et al., 2003). We stirred the dry sediment mixture with a whisk to assure a reasonably homogeneous clay distribution within the sample and packed the sample using slow, dry pluviation (Germaine & Germaine, 2009). We calculated the gravimetric porosity of the sample (ϕ_{grav}) from the mass of sediment, the total sample volume (V_{tot}), and the solid grain density (ρ_s = 2.65 g/mL). We secured the sample inside the pressure vessel, filled the vessel with confining fluid, and transferred it to the vertical hanger frame.

While in the vertical position, we used two vacuum pumps to create a small pressure gradient within the sample that induced upward brine flow and pulled five pore volumes of brine through the sample. We collected the brine downstream and confirmed that no clay was entrained in the effluent brine. We then raised the pore (P_{pore}) and confining pressures to experimental conditions (Table 1), using the outlet and confining pumps, and measured the Skempton coefficient ($\beta = \Delta P_{pore}/\Delta P_{conf}$) (Skempton, 1954). The β-value was always greater than 0.85 after pressurization, suggesting that a negligible amount of gas remained in the sample.

Table 1
Summary of Experimental Parameters

Test name	Porosity, ϕ_{grav}	Salinity, C_j (wt % NaCl)	Pressure, P_{pore} (MPa)	Conf. pressure, P_{conf} (MPa)	Temp, T_{conf} (°C)	CT[a]
Gas-1	0.39	7	12.24	12.93	14.7	Y
Hydrate-1	0.41				1.01	Y
Hydrate-2	0.38				1.05	N
Hydrate-3	0.39				1.02	N

[a]Experiments performed in the CT scanner.

We performed constant flow permeability tests (Olsen, 1966) at flow rates ranging from 5 to 50 mL/min on two brine-saturated samples at our experimental conditions. We determined that these samples had an intrinsic permeability of 4.9 ± 0.4 Darcy, which is a reasonable value for clean sand packs with approximately 40% porosity (Davis & DeWiest, 1967; Onur, 2014; West, 2010).

2.3 Experimental Procedure

With the pore pressure (P_{pore}) at the experimental condition (Table 1), we pressurized the inlet pump to match P_{pore} but kept the brine and methane separated at the inlet valve (Figure 1: red valve), outside the hydrate stability zone (Figure 1: red dashed box). We then cooled the sample to the experimental temperature (Table 1) and, prior to starting the experiment, identified and reduced any fluid leaks to less than 2% of the drainage rate. We then opened the inlet valve, bringing gas in contact with the brine, and rapidly (1 mL/min) removed enough brine to bring gas in direct contact with the sample. The gas and brine in the tubing were at room temperature during this process, which makes it very unlikely that hydrate formed within the tubing upstream of the sample. We then removed brine from the base of the sample at a constant rate (0.18 mL/hr) and maintained a constant gas pressure. We ended the experiments when the CT-derived low bulk density front (gas or hydrate) reached the sample outlet in order to maintain confidence in the masses of methane and brine in the sample.

2.4 Experimental Parameters

We performed one gas flood (two-phase) experiment and three hydrate formation (three-phase) experiments (Table 1). We saturated the samples with a 7 wt % NaCl brine to reduce the predicted three-phase equilibrium hydrate saturation (S_{heq}) from 84% to 67%. We maintained a constant effective stress ($P_{eff} = P_{conf} - P_{pore}$) of 0.7 MPa to limit sand migration and flow along the sample-sleeve boundary.

The maximum temperature at which hydrate is stable at the experimental pressure and salinity conditions is 11.5°C (Liu & Flemings, 2007). The gas flood experiment, Gas-1, was kept 3.2°C greater than the hydrate stability temperature (Table 1). The hydrate formation experiments, Hydrate-1, Hydrate-2, and Hydrate-3, were kept 10.5°C below the stability temperature (Table 1), to encourage rapid hydrate nucleation (Rees et al., 2011; Seol & Kneafsey, 2009; You, Kneafsey, et al., 2015).

2.5 X-ray Computed Tomography Scan Methods

We performed the gas flood (Gas-1) and one hydrate formation experiment (Hydrate-1) within a medical CT scanner. We collected scans, prior to the experiment, of the sample filled with only methane (dry) and only brine (wet) and then collected scans at least every 24 hr throughout the experiment. Each scan consisted of prismatic voxels (3 mm × 0.23 mm × 0.23 mm) approximately one grain wide and six grains long.

We determined the sample porosity (ϕ_{CT}) of each voxel using the CT attenuations measured in the wet (CT^{wet}) and dry (CT^{dry}) samples (Appendix Appendix A):

$$\phi_{CT} = \frac{CT^{wet} - CT^{dry}}{CT^{l-g}}. \quad (1)$$

CT^{l-g} is equal to the difference in CT attenuations of pure brine and methane. We calibrated this value by assuming that the CT-derived porosity, averaged over the entire sample, equaled the gravimetric porosity (Appendix Appendix A). We used the CT porosity from each voxel (ϕ_{CT}), the grain density (ρ_s), and the fluid (ρ_l = 1.063 g/cm^3) density (Hassanzadeh et al., 2008; Pitzer, 1991) to calculate the bulk density of every voxel when only brine ( ) or methane ( ) was present in the sample. We linearly interpolated between these endpoint values to determine the bulk density of each voxel in each scan taken during the experiment ( ):

$$\rho_b^{exp} = \left[\rho_b^{dry} + \left(\left(\rho_b^{wet} - \rho_b^{dry}\right) \cdot \left(\frac{\left(CT^{exp} - CT^{dry}\right)}{\left(CT^{wet} - CT^{dry}\right)}\right)\right)\right]. \quad (2)$$

We calculated the methane gas phase saturation (S_g) in each voxel in Gas-1 using linear interpolation between the experimental bulk density and the bulk density endpoints of each voxel:

$$S_g = \frac{\left(\rho_b^{exp} - \rho_b^{wet}\right)}{\left(\rho_b^{dry} - \rho_b^{wet}\right)}. \quad (3)$$

We also used the CT scans to determine the affected voxels, defined by where the change in sample bulk density ($\Delta\rho_b = \rho_b^{exp} - \rho_b^{wet}$) exceeded the CT scanner measurement error (±0.024 g/mL; Appendix Appendix B). With a porosity of 40%, 0.024 g/mL equates to replacing the brine in a voxel with either 6% gas or 38% hydrate. We determined the pore volume of the affected voxels by multiplying the voxel volume (1.8 × 10^{-4} mL) by the initial porosity of each affected voxel (ϕ_{CT}). We then calculated the total affected volume (V_{aff}) as the sum of the individual pore volumes of each affected voxel. The affected volume may be underestimated by between 0.5 and 2.6 mL due to the fluid dispersion grooves in the sample endcap and an approximately 1-mm buffer between the endcap and the first CT slice. This error decreases throughout the experiment, however, relative to the total estimated affected volume.

3 Results

3.1 Sample Porosity

The CT-derived porosity (equation 1) in Gas-1 (Figure 2a: red line) and Hydrate-1 (Figure 2a: green line) decreased downward from 43.5% to 38% and 39%, respectively. Sediment compaction during packing resulted in low porosity regions near the sample outlets and sample handling created narrow, high porosity fingers extending down the edges of the samples (Figures 2b and 2c).

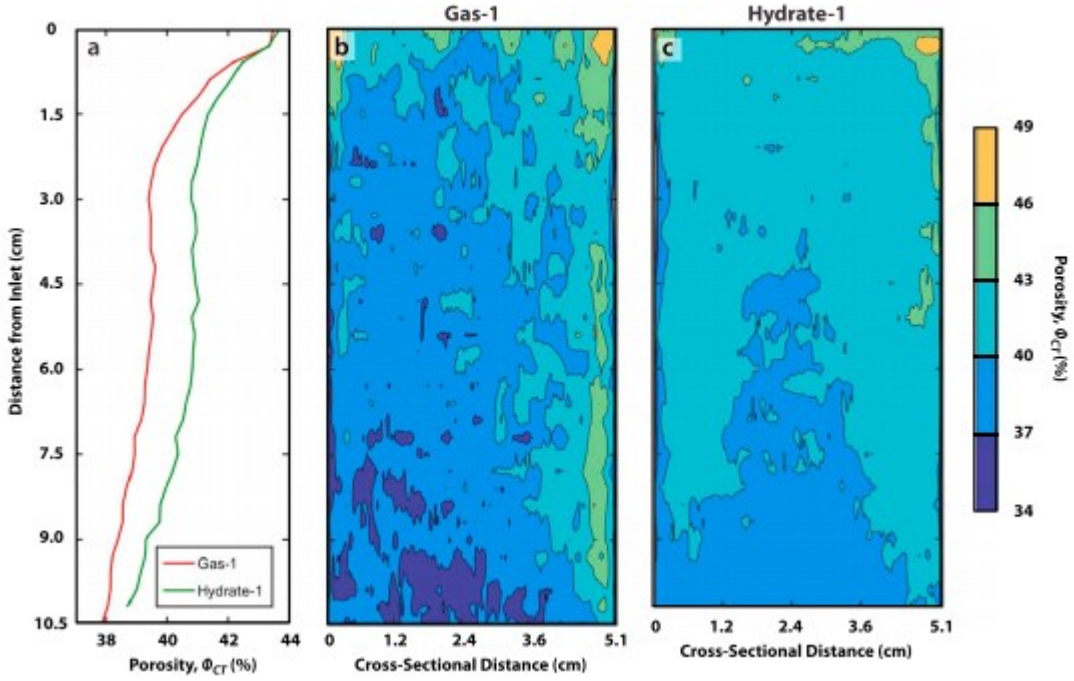

Figure 2

Computed tomography (CT)-derived initial porosity of samples used in the Gas-1 and Hydrate-1, calculated from the dry and wet scans (equation 1). (a) CT porosity, averaged across each slice, with distance from the inlet in Gas-1 (red line) and Hydrate-1 (green line). (b and c) Porosity along the center plane of the sample in Gas-1 and Hydrate-1.

3.2 Pressure Differentials

In Gas-1, no significant pressure differentials ($dP = P_{in} - P_{out}$) across the sample were observed (Figure 3a: red line). In the hydrate formation experiments, however, temporary pressure differentials continuously formed and dissipated (Figure 3a: green line). Since the gas pressure was held constant, these differential pressures were the result of decreasing brine pressure. Individual pressure differentials increased at approximately 0.18 MPa/hr before exceeding some critical value and decreasing rapidly (Figure 3b: green line). Typically, the samples maintained a differential pressure of approximately 0.1 MPa throughout the experiments but reached maximum values in Hydrate-1, Hydrate-2, and Hydrate-3 of 0.48, 0.25, and 0.69 MPa, respectively. Differential pressure development was correlated with a significant reduction in the gas flow rate and, when the differential pressure dissipated, was followed by rapid gas flow into the sample (Figure 3b: black line).

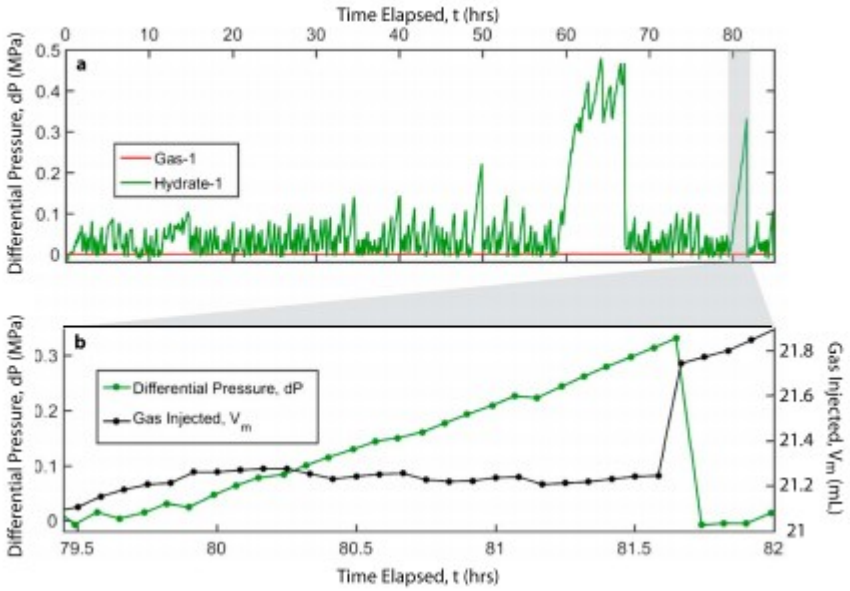

Figure 3

Differential pressure (*dP*) development in Hydrate-1. Similar behavior was observed in all hydrate formation experiments. (a) Differential pressure results from both Gas-1 (red line) and Hydrate-1 (green line). Temporary pressure differentials, not observed in Gas-1, developed throughout Hydrate-1. (b) Development of a single pressure differential in Hydrate-1 compared to the volume of methane injected during the same period.

3.3 Fluid Volumes

In Gas-1, the volume of methane injected (V_m; Figure 4: red line) was always approximately equal to the volume of brine removed (V_l; Figure 4: dashed black line). In the hydrate experiments (Figure 4: green, pink, and blue lines) the methane injected always exceeded the brine removed within the first 1.5 hr of the experiment and, after 85 hr, an average of 22.6 ± 1 mL of methane had been injected into the samples. Fluctuations in the volume data were driven by minor ambient temperature variations.

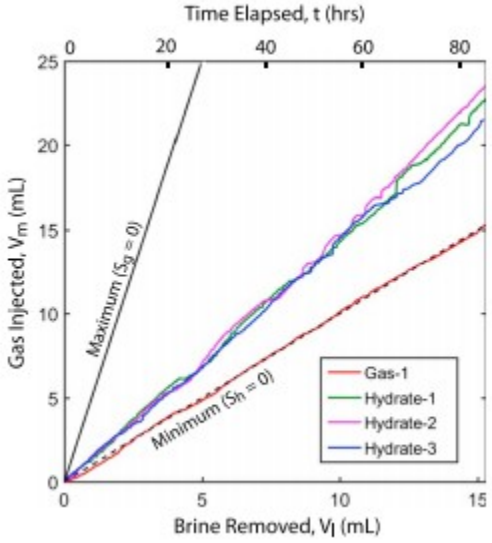

Figure 4

Comparison of the volumes of the methane injected during the gas flood (red line) and hydrate formation experiments (green, pink, and blue lines) compared to experimental minimum (dashed black line) and maximum (solid black line) end-members (Appendix C).

3.4 CT-Derived Bulk Density

In Gas-1, the bulk density decrease exceeded the CT error (Figure 5a: red dashed line) within the upper 2 cm, after 48 hr (Figure 5a: black dashed line), and the upper 3 cm, after 83 hr (Figure 5a: black dotted line). The gas saturation (equation 3) near the inlet increased from 61% to 66%, between 48 and 83 hr, and always decreased downward. Gas flow was primarily concentrated along a narrow finger at the edge of the sample (Figures 5b–5d) coincident with a zone of high initial porosity (Figure 2b).

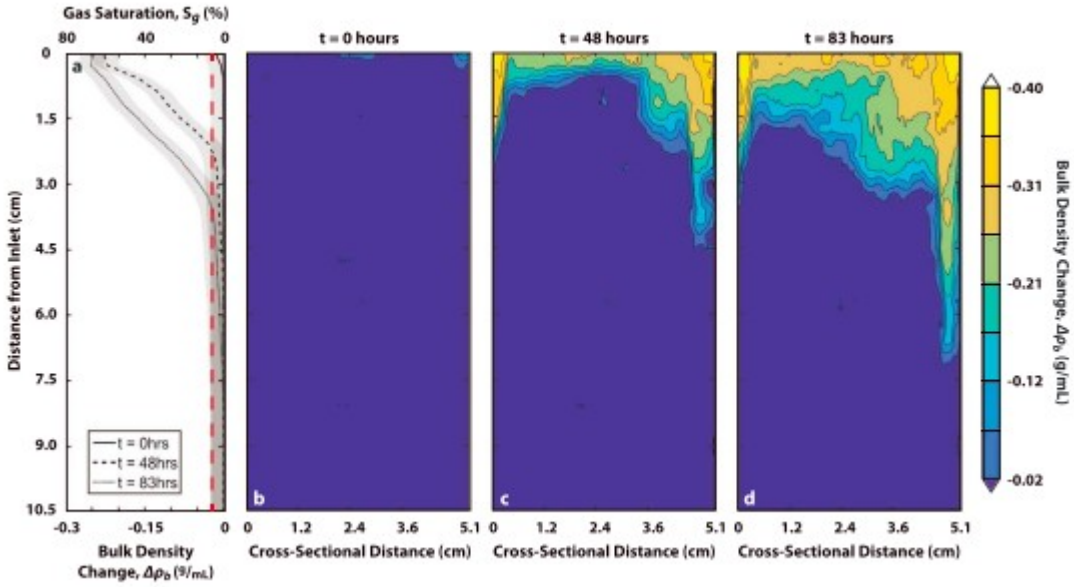

Figure 5

Evolution of the change in computed tomography (CT)-derived bulk density (equation 2) during Gas-1. (a) Bulk density change, averaged across each slice, as a function of distance from the inlet. Gas saturation is calculated using equation 3, assuming a porosity of 40%. The dashed red line indicates the CT measurement error (section 2.5), and the shaded regions indicate one standard deviation in the CT data. (b–d) Two-dimensional change in bulk density along the center plane of the sample after 0, 48, and 83 hr elapsed.

At the beginning of Hydrate-1, the bulk density decrease exceeded the CT error (Figure 6a: red dashed line) within the top 0.5 cm of the sample (Figure 6a: solid black line) due to gas injection during experiment initialization. This decrease was concentrated in the upper corners of the sample (Figure 6b) where the initial porosity was high (Figure 2c). After 48 hr, the bulk density decreased in the region from 0 to 3.6 cm (Figure 6a: dashed black line) throughout the center of the sample (Figure 6c). Below 3.6 cm, there was flow both down the sample edge and across the sample (Figure 6c). After 85 hr, the bulk density decreased within the region from 3.5–7 cm (Figure 6a: dotted black line), relative to 48 hr elapsed, primarily in the center of the sample and along the opposite edge from the original preferential flow (Figure 6d).

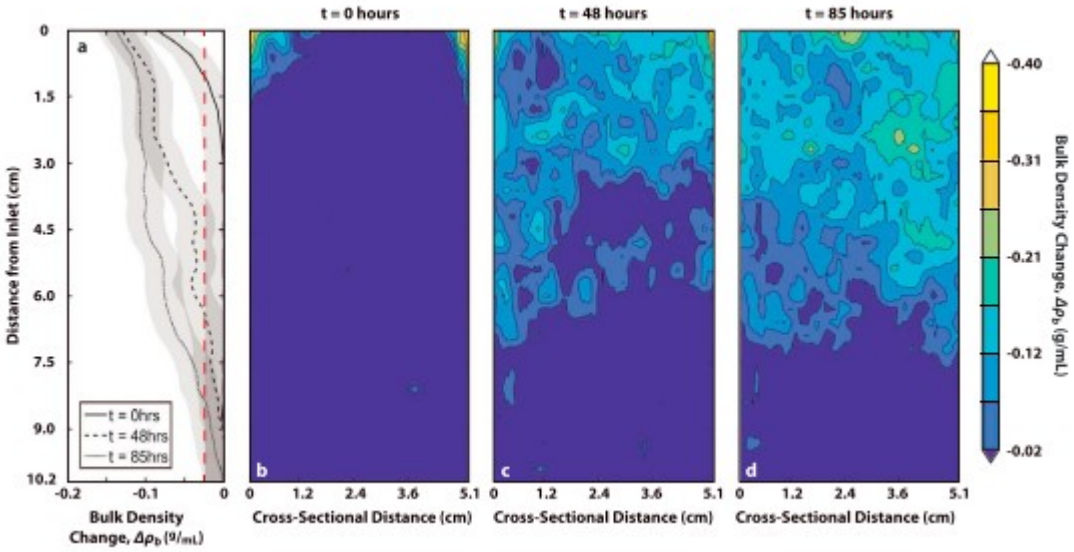

Figure 6

Evolution of the change in computed tomography (CT)-derived bulk density (equation 2) during Hydrate-1. (a) Bulk density change, averaged across each slice, as a function of distance from the inlet. The dashed red line indicates the CT measurement error (section 2.5), and the shaded regions indicate one standard deviation in the CT data. (b–d) Two-dimensional change in bulk density along the center plane of the sample after 0, 48, and 85 hr elapsed.

3.5 Affected Volumes

In Gas-1, the affected volume (V_{aff}; section 2.5) increased to 25.4 mL by the end of the experiment (Figure 7: red dots) at approximately 0.3 (Figure 7: dashed red line) mL/hr. In contrast, in Hydrate-1, the affected volume increased to 60.1 mL by the end of the experiment (Figure 7: green dots) at approximately 0.7 (Figure 7: dashed green line) mL/hr.

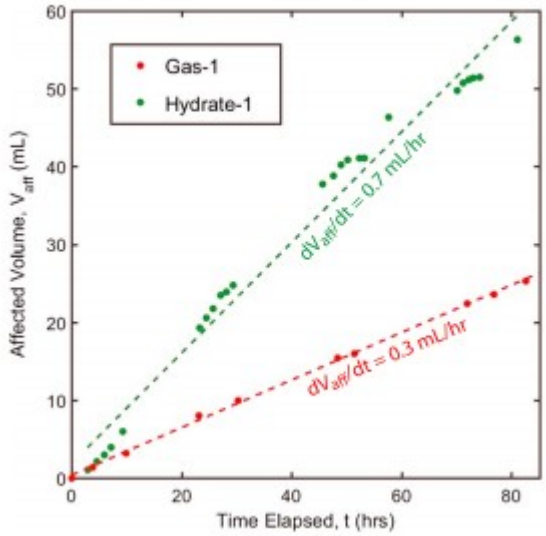

Figure 7

Affected volume during Gas-1 (red dots) and Hydrate-1 (green dots). The dashed lines indicated the best fit linear trends for each experiment.

4 Mass Balance Analysis

We use mass balance (Appendix Appendix C) to determine the relationship between the volumes of gas injected and brine removed and the amount of hydrate and gas present in the sample (Figure 8). We assume that (1) the brine density is constant (maximum density increase due to elevated salinities is 13% of the initial density), (2) the mass of methane dissolved in the brine is negligible, and (3) the pore volume is constant (confirmed by monitoring the confining pump volume and axial CT slice radii).

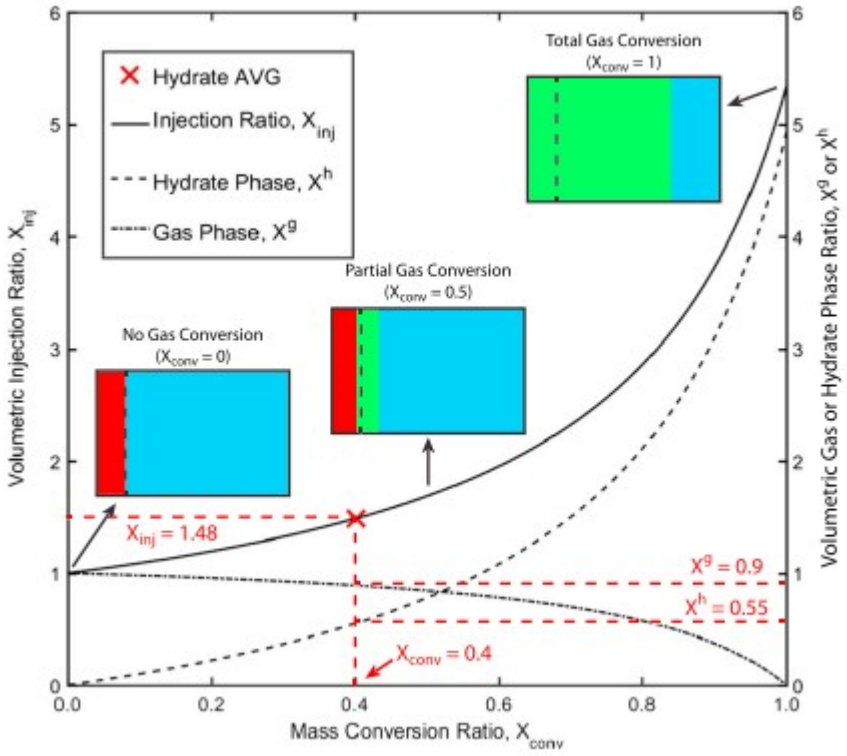

Figure 8

Volumetric injection ratio (X_{inj}; solid line) and volumetric hydrate (X^h; dashed line) and gas (X^g; dot-dashed line) phase ratios as a function of the mass conversion ratio (X_{conv}). The red dashed lines show the average X_{conv}, X_{inj}, X^g, and X^h at the final state of the hydrate experiments (red cross). The inset images show normalized gas (red), hydrate (green), and liquid (blue) phase volumes in a unit cell with X_{conv} equal to 0, 0.5, and 1. The black dashed line in each inset image indicates the original volume of brine removed from the unit cell.

We convert the volumes of methane injected (V_m) and brine removed (V_l) during each experiment (Figure 4) into an equivalent methane (m_m) and water (m_w) mass. m_m must be equal to the mass of methane gas (m_m^g) plus the mass of methane in the hydrate (m_m^h) in the sample ($m_m = m_m^g + m_m^h$). m_w must be equal to the original mass of water in the sample (m_{wi}) minus the masses of water in liquid (m_w^l) and hydrate (m_w^h) in the sample ($m_w = m_{wi} - m_w^l - m_w^h$). We calculate m_m^g and m_m^h from mass balance (Appendix C) and convert these values into equivalent volumes of the free gas (V^g) and hydrate (V^h) using the phase densities and stoichiometry (Table E1).

From this mass balance, we define the following ratios (Appendix C): (1) The mass conversion ratio ($X_{conv} = m_m^h/m_m$) is the ratio of the mass of methane converted to hydrate to the total mass of methane injected; (2) the volumetric injection ratio ($X_{inj} = V_m/V_l$) is the ratio of the volume of methane injected to the volume of brine removed (Figure 8: solid line); (3) the volumetric gas phase ratio ($X^g = V^g/V_l$) is the ratio of the volume of methane gas in the sample and the volume of brine removed (Figure 8: dot-dashed line); and (4) the volumetric hydrate phase ratio ($X^h = V^h/V_l$) is the ratio of

the volume of hydrate in the sample and the volume of brine removed (Figure 8: dashed line).

With no gas conversion ($X_{conv} = 0$), the volume of methane injected equals the volume of brine removed ($X_{inj} = 1$) and all the methane is in the gaseous phase ($X^g = 1$; $X^h = 0$). With total gas conversion into hydrate ($X_{conv} = 1$), the volume of methane injected is 5.34 times the volume of brine removed ($X_{inj} = 5.34$), there is no gaseous phase ($X^g = 0$), and there is 4.93 times more hydrate present than brine removed ($X^h = 4.93$). These cases represent the minimum (Figure 4: dashed black line) and maximum (Figure 4: solid black line) hydrate formation scenarios for our experiments. An injection ratio between these end-members indicates partial gas conversion into hydrate and the presence of both methane gas and hydrate in the sample at a particular volumetric ratio.

In Gas-1, X_{inj} was always approximately 1 (Figure 9: red line), indicating that no hydrate formed in the sample ($X_{conv} = 0$) and that gas directly replaced brine ($X^g = 1$; $X^h = 0$), as expected. In the hydrate experiments, X_{inj} and X_{conv} slowly increased (Figure 9: green, pink, and blue lines), to final values, averaged across all experiments, of 1.48 ± 0.06 and 0.40 ± 0.03, respectively (Figures 8 and 9: red cross), indicating that both gas and hydrate were present in the sample throughout the experiments. At this conversion ratio, the volumetric gas ($X^g = 0.90$) and hydrate ($X^h = 0.55$) phase ratios at the end of the experiments (Figure 8) indicate that the combined volume of gas and hydrate in the sample was 1.45 times greater than the volume of brine removed.

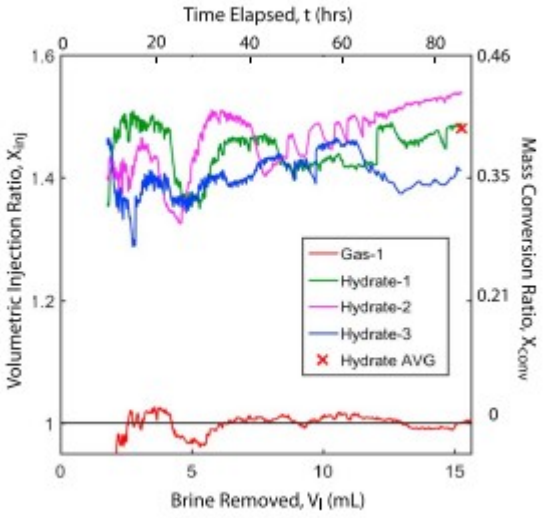

Figure 9

Comparison of volumetric injection (X_{inj}) and mass conversion (X_{conv}) ratios during the gas flood (red line) and hydrate formation (green, pink, and blue lines) experiments (Appendix C). The red cross indicates the average X_{conv} and X_{inj} and the end of the hydrate experiments. Decrease in X_{conv} in Hydrate-3 after 62 hr was caused by a persistent gas flow blockage.

We calculate the bulk phase saturations of the methane gas (S_g), liquid brine (S_l), and solid hydrate (S_h) within the affected volume (V_{aff}) in our experiments using mass balance (Appendix Appendix D):

$$S_g = \frac{\frac{\rho_h}{M_h}\left(\frac{\rho_g M_w N V_m}{(1-C_l)} + \rho_l M_m V_l\right) - \rho_g \rho_l V_m}{V_{\text{aff}}\left(\frac{\rho_h}{M_h}\left(\frac{\rho_g M_w N}{(1-C_l)} + \rho_l M_m\right) - \rho_g \rho_l\right)}, \quad (4)$$

$$S_l = 1 - S_g + \frac{\rho_g M_h}{M_m \rho_h}\left(S_g - \frac{V_m}{V_{\text{aff}}}\right), \quad (5)$$

and

$$S_h = 1 - S_g - S_l. \quad (6)$$

This calculation is susceptible to changes in the gas volume due to ambient temperature fluctuations and to the underestimation of V_{aff} (section 2.5). These errors are greatest near the beginning of the experiments when V_{aff} is smaller.

In Gas-1, the mass balance-derived bulk gas (Figure 10a: red dots), brine (Figure 10a: blue dots), and hydrate (Figure 10a: green dots) phase saturations within the affected volume reached steady state values of 58%, 42%, and 0%, respectively. The CT-derived bulk gas saturation (Figure 10a: red triangles) within the affected volume also increased to 58% during the experiment. The eventual agreement between the mass balance and CT-derived gas saturations indicates that the affected volume, at least in a gas-brine system, is an accurate measure of the volume containing gas. We assume this relationship extends to the gas-brine-hydrate system as well.

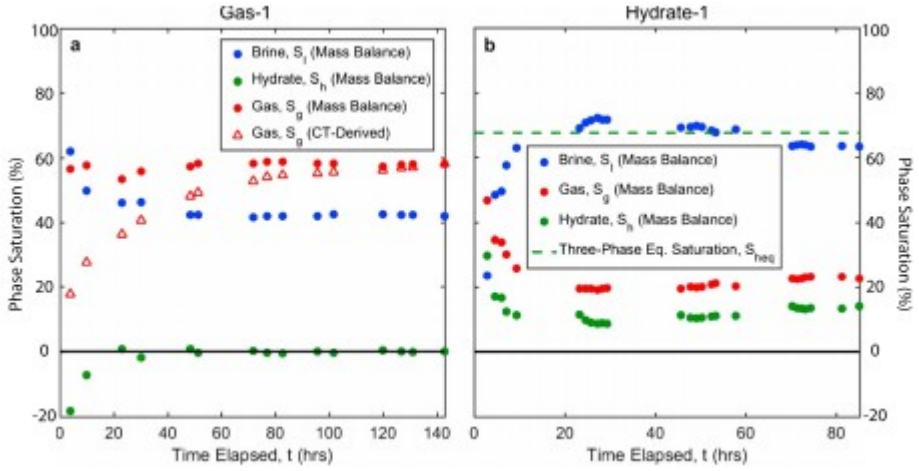

Figure 10

Bulk phase saturations within the affected volume during Gas-1 and Hydrate-1. (a) Mass balance-derived bulk gas (red dots), brine (blue dots), and hydrate (green dots) phase saturations compared to the computed tomography-derived bulk gas phase saturation (red triangles) within the affected volume during Gas-1. (b) Mass balance-derived bulk brine (blue dots), hydrate (green dots), and gas (red dots) phase saturations within the affected volume during Hydrate-1. The dashed green line

represents the bulk hydrate saturation required to elevate the bulk salinity to the three-phase equilibrium concentration.

In Hydrate-1, between 23 and 85 hr, the average mass balance-derived bulk gas (Figure 10b: red dots), brine (Figure 10b: blue dots), and hydrate (Figure 10b: green dots) saturations within the affected volume were 21%, 68%, and 11%, respectively. Compared to Gas-1, this indicated that hydrate formation in the sample resulted in a decrease in the amount of free gas present and an increase in the amount of brine remaining in the affected volume.

Liu and Flemings (2006) indicated that salt exclusion during hydrate formation raises the bulk salinity ($C = C_i/[1 - S_h]$) as a function of the hydrate saturation (S_h) and the initial salinity (C_i). The average S_h in the affected volume in Hydrate-1 is 11%, which would elevate the brine salinity to 8.1 wt % NaCl in that region. This indicates that both the bulk salinity and the hydrate saturation during Hydrate-1 were far below the three-phase equilibrium values (C_{eq} = 21 wt % NaCl; S_{heq} = 68%).

5 Discussion

Our results illuminate how hydrate forms during gas injection into porous media at the core-scale. We interpret that, during injection, a hydrate skin forms at the gas-brine interface and separates the gas from the brine. As a result, the gas, hydrate, and brine are not at thermodynamic equilibrium. The formation of a hydrate skin has been demonstrated experimentally at the pore-scale (Davies et al., 2010; Jin et al., 2012; Katsuki et al., 2007; Taylor et al., 2007). Our contribution is to demonstrate how this microscale phenomenon controls gas flow and hydrate formation at the macroscale.

We show that hydrate formation occurs rapidly and consistently at our experimental conditions (Figure 4), temporary flow blockages develop (Figure 3), and hydrate and gas are distributed throughout the sample (Figure 6). Approximately 40% of the methane injected during the hydrate experiments is converted into hydrate (Figure 9), which results in an average hydrate saturation within the affected volume of 11% (Figure 10b). This saturation is much less than the hydrate saturation predicted assuming three-phase equilibrium, which is 67% (Figure 10b: green dashed line). The brine saturation within the affected volume (Figure 10) in the hydrate experiments (68%) is much greater than in the gas flood experiment (42%). We present a conceptual hydrate formation model (Figure 11) and a one-dimensional diffusion model (Figure 12) that captures these macroscale observations.

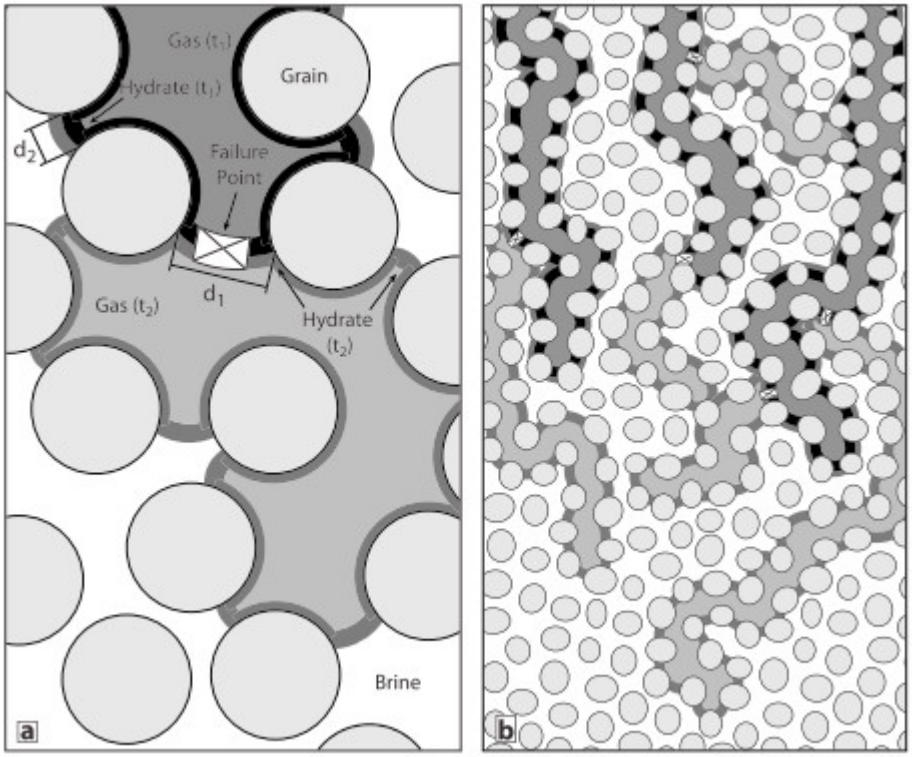

Figure 11

Conceptual model of gas progression and hydrate skin growth at the pore- and core-scales. (a) At the pore-scale, between times t_0 and t_1, gas flows through the pores until it reaches mechanical equilibrium with the brine. A solid hydrate skin then forms at the gas-brine interface and blocks flow. Between t_1 and t_2, methane diffuses through the skin, forming additional hydrate as a differential pressure develops across the skin. At t_2, the hydrate skin fails and gas progresses farther into the sample, forming a new hydrate skin. (b) At the core-scale, multiple interconnected gas flow paths, encased in hydrate skins, progress through the sample over time.

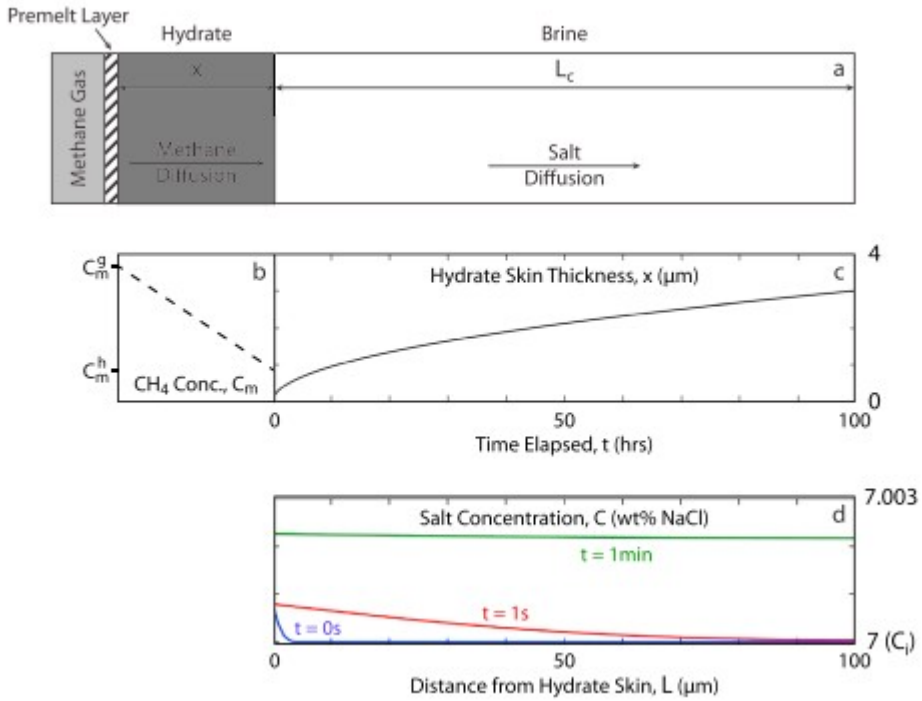

Figure 12

One-dimensional model of hydrate formation and salinity evolution (Appendix E). (a) Cartoon of the model domain. Gas and brine are separated by a hydrate skin. Gas and hydrate are separated by a thin, liquid layer (premelt). The brine phase has a characteristic length (L_c). The hydrate skin increases in thickness (x) as methane diffuses across the hydrate. (b) Methane concentration profile across the hydrate (dashed line). (c) Hydrate skin thickness over time (solid line) calculated using equation 7. (d) Salt concentration in the brine after 0 s (blue line), 1 s (red line), and 1 min (green line) elapsed ($D_m = 10^{-15}$ m^2s^{-1}; L_c = 100 μm).

5.1 Macroscale Hydrate Formation Model

In the hydrate formation experiments, hydrate nucleates rapidly at the gas-brine interface, forming a continuous hydrate skin that blocks the pore throats along the flow path and, periodically, blocking flow entirely (Figure 11a). After blockage, continued brine removal increases the pressure differential across the hydrate skin until it fails at the weakest point. Gas then flows into the sample until the gas and brine reach mechanical equilibrium. Subsequently, hydrate nucleates and a new hydrate skin forms over time with the rate limited by nucleation kinetics and/or the rate that the hydrate solidifies into an impermeable skin (Natarajan et al., 1994; Skovborg et al., 1993; Taylor et al., 2007). Through this process, gas is distributed and hydrate forms throughout the sample (Figure 11b). There was higher brine saturation (Figure 10) within a larger affected volume (Figure 7) in Hydrate-1, compared to Gas-1. We interpret that the hydrate skin blocks gas access to a larger fraction of the pores and forces gas farther into the sample than would occur without hydrate.

5.2 Pore-Scale Hydrate Skin Growth

The hydrate skin separates the brine and gas and limits hydrate formation to the rate that methane can diffuse through the solid hydrate (Taylor et al., 2007). We describe this process with a one-dimensional model where methane is transported by diffusion through a liquid phase within the microporous hydrate (Kuhs et al., 2000; Kuhs et al., 2004). Between the methane gas and the hydrate, there is a thin, metastable, liquid layer (Figure 12a), similar to the premelted water observed in ice-air systems (Dash et al., 2006; Rempel et al., 2004), into which methane gas dissolves. The methane concentration at the gas-hydrate interface equals the methane gas solubility in water (C_m^g) because there is an abundance of methane gas and no water to form hydrate. The methane concentration at the brine-hydrate interface equals the hydrate solubility in water (C_m^h) because the local concentration must be in equilibrium with hydrate.

In this model, the hydrate skin thickness (x) increases with the square root of time (Appendix E1):

$$x = \sqrt{\frac{2D_m M_h \left(C_m^g - C_m^h\right)}{\rho_h}}\sqrt{t}. \quad (7)$$

The methane concentration gradient ($dC_m = \left[C_m^g - C_m^h / x\right]$; Figure 12b), the diffusion coefficient of methane through hydrate (D_m), and time control the hydrate skin thickness (equation 7). D_m can range from 10^{-14} m^2 s^{-1} (Davies et al., 2010) to 10^{-16} m^2 s^{-1} (Genov et al., 2004; Kuhs et al., 2006). For a value of D_m equal to 10^{-15} m^2 s^{-1}, the hydrate skin thickness (Figure 12c) is 0.04 μm after 1 min, 0.28 μm after 1 hr, and 2.6 μm at our experimental time scale (85 hr). Over this period, the growth rate decreases 70-fold due the increasing length scale through which methane must diffuse (Figure 12c).

We independently estimate the average hydrate skin thickness (x_{avg}) from the hydrate saturation (S_h), the gravimetric porosity (ϕ_{grav}), and the gas-brine interfacial area per porous medium volume (A_i):

$$x_{avg} = \frac{\phi_{grav} S_h}{A_i}. \quad (8)$$

Brusseau et al. (2006, 2007) experimentally determined the relationship between the water saturation (S_l) and the interfacial area in sand packs during drainage. This area increases linearly with the water saturation with a slope dependent upon the grain size. For the sand used in this study A_i, in units of cm^{-1}, is calculated by:

$$A_i = 147[1 - S_l]. \quad (9)$$

This relationship is robust for both imbibition and drainage, which have fundamentally different pore-filling processes. Therefore, we can assume that this relationship is also applicable to the intermittent gas flow in our experiments. The brine saturation at the end of Hydrate-1, prior to hydrate

formation ($S_l = 1 - S_g$), is 77%, which indicates an A_i equal to 34 cm^{-1} (equation 9). From equation 8, we calculate that x_{avg} equals 13.3 μm at the end of Hydrate-1. This value is greater than predicted by our diffusion model (2.8 μm) at our experimental time scale but is similar to experimental observations (Taylor et al., 2007) of hydrate skins between 10 and 60 μm thick.

We interpret that, initially, hydrate formation occurs more rapidly than described by diffusion but decreases dramatically once the hydrate skin fully solidifies as has been observed (Davies et al., 2010; Taylor et al., 2007). It is also possible that the methane concentration gradient through the hydrate may be controlled by the hydrate cage occupancy in the presence of excess gas and excess water. This condition would increase the difference in methane concentration by a factor of 7.2 (Huo et al., 2003), which would increase the hydrate growth rate by a factor of 2.7; this increase results in a skin thickness of 7.6 μm after 85 hr, using the same parameters as above. While these results suggest that the early formation process is more complicated than can be described by simple diffusion, the net behavior is that a very thin hydrate skin forms quickly and that methane transport is very limited once this hydrate forms. As a result, the skin is thicker near the inlet, where it is older, and thinner at the outlet, where it is younger.

5.3 Salinity at Brine-Hydrate Interface

As hydrate forms at the brine-hydrate interface, salt is excluded and the local salinity increases. The salt concentration gradient drives salt diffusion away from the hydrate and competes with the hydrate-driven salt flux to control the local salinity. We derived a salt flux that decreases with time and is equal to the mass of salt excluded by hydrate formation (Appendix E2). We then solve for the salt concentration with distance from the hydrate over time with this salt source using Laplace transformation (Appendix E3). We assume a $D_m$equal to 10^{-15} m^2 s^{-1} and a characteristic length (L_c) of 100 μm (approximately one third of a grain diameter). Immediately after initial hydrate formation (Figure 12d: blue line), the salinity increases at the brine-hydrate boundary, producing a concentration gradient near the hydrate skin that causes NaCl to diffuse away from the hydrate. As the hydrate skin grows, the hydrate formation rate and, subsequently, the salt source decline. As a result, the salt gradient dissipates rapidly and the salinity rises across the characteristic length at an approximately uniform concentration (Figure 12d: red, green, and pink lines). By the end of our experiments (85 hr), the bulk salinity reaches 7.2 wt % NaCl, which is far below C_{eq}(21 wt % NaCl).

Increasing hydrate formation rate, through a larger D_m or dC_m or longer characteristic length, does not change the fundamental behaviors of the model: The salt loss due to diffusion quickly exceeds the salt source due to hydrate formation. As a result, we envision that the brine adjacent to the hydrate is well-mixed with approximately uniform but gradually increasing

salinity. This model shows that hydrate formation is primarily limited by methane diffusion across the hydrate skin.

5.4 Field Scale and Modeling Implications

The rapid diffusion of salt away from the hydrate skin produces different thermodynamic states on either side of the skin. On the gas side, hydrate, premeltwater (Figure 12a), and methane gas are present in three-phase equilibrium. On the brine side, hydrate and brine at a salinity well below the three-phase concentration are present in two-phase equilibrium. Since methane transport through the skin is very slow, these states can coexist for tens to thousands of years. This transport limitation provides a mechanism for gas to coexist with water and hydrate at the pore-scale within systems that are generally assumed to be at two-phase (liquid-hydrate) equilibrium conditions.

The formation of the hydrate skin, however, does not significantly impede gas flow through the sample. In our experiments, flow was maintained with the development of a pressure differential of approximately 0.1 MPa. In the field, the collection of a continuous, 10-m gas column which; this is not an uncommon occurrence in active hydrocarbon regions (Boswell, Frye, et al., 2012; Frye et al., 2012), would provide this pressure gradient. Thus, this mechanism could explain vertical gas migration far above the base of hydrate stability without requiring bulk thermodynamic equilibrium. This behavior is similar to a nonequilibrium flow model recently presented by Fu et al. (2018) and to hydrate formation on the walls of a fracture separating gas and water within the hydrate stability zone (Ginsburg & Soloviev, 1997; Riedel et al., 2006).

This behavior could generate the high hydrate saturations observed in the field. The hydrate saturation that we observed at laboratory time scales is low (11%), compared to field observations (60–90%). However, methane will continue to diffuse through the skin and form additional hydrate at the brine-hydrate interface. Over thousands of years this could significantly increase the bulk hydrate saturation. Additionally, we suspect this saturation is strongly dependent on the flow rate and expect lower flow rates, such as those observed in the field (Liu & Flemings, 2007; Torres et al., 2002), to produce higher hydrate saturations.

Finally, these results suggest that models that assume the gas, hydrate, and brine are at thermodynamic equilibrium at the core-scale and larger (Darnell & Flemings, 2015; Liu & Flemings, 2007; Reagan & Moridis, 2008, 2009; Torres et al., 2004) may not capture the behaviors of gas transport and hydrate formation within the hydrate stability zone. A fundamental challenge is to incorporate the core-scale behaviors we observed into field-scale models that describe hydrate formation in geologic systems.

6 Conclusions

We injected free methane gas into a brine-saturated sand pack under hydrate-stable conditions to form methane hydrate and observed temporary flow blockages throughout the experiments. On average, hydrate and free gas occupied 11% and 21% of the pore space, respectively. This hydrate saturation is much lower than predicted when assuming gas, hydrate, and brine are at three-phase equilibrium in the sample (67%). We interpret that as free gas enters the sample, hydrate nucleates rapidly at the gas-brine interface and forms a continuous barrier that separates the gas and brine phases. Occasionally, the hydrate skin fails due to the development of a significant pressure differential across the skin. This behavior leads to low saturations of gas and hydrate distributed throughout the sample.

A long-standing question is how free gas migrates through the hydrate stability zone in geologic systems. We suggest that gas flow is assisted by the mechanical separation of gas and brine phases by a hydrate skin. Where gas is present, there is three-phase equilibrium (gas, premelt, and hydrate), and, where brine is present, there is two-phase equilibrium (brine and hydrate). Methane slowly diffuses through the hydrate from the gas to the brine and forms additional hydrate at the brine-hydrate interface. Over geologic time, this transport process could result in high hydrate saturations distributed throughout the reservoir, as is observed in the field.

Nomenclature

Symbol	Name	Dimension	Unit
A_i	Interfacial area per porous media volume	(L^{-1})	(cm^{-1})
C	Salinity	$(M\,M^{-1})$	(wt %)
C_{eq}	Three-phase equilibrium salinity	$(M\,M^{-1})$	(wt %)
C_i	Initial salinity	$(M\,M^{-1})$	(wt %)
C_m	Methane concentration	$(M\,L^{-3})$	$(mol\,m^{-3})$
C_m^g	Solubility of methane in water	$(M\,L^{-3})$	$(mol\,m^{-3})$
C_m^h	Solubility of hydrate in water	$(M\,L^{-3})$	$(mol\,m^{-3})$
CT^{avg}	Average CT attenuation of wet and dry sample	(–)	(Houndsfield)
CT^{dry}	CT attenuation value of dry sample	(–)	(Houndsfield)
CT^{err}	CT attenuation error	(–)	(Houndsfield)
CT^{exp}	Experimental CT attenuation value	(–)	(Houndsfield)
CT^{l-g}	Brine-methane CT attenuation contrast	(–)	(Houndsfield)
CT^{wet}	CT attenuation value of wet sample	(–)	(Houndsfield)
D_c	Diffusion coefficient of salt in water	$(L^2\,T^{-1})$	$(m^2\,s^{-1})$
D_m	Diffusion coefficient of methane through hydrate	$(L^2\,T^{-1})$	$(m^2\,s^{-1})$
dC_m	Methane concentration gradient	$(M\,L^{-3}\,L^{-1})$	$(mol\,m^{-3}\,m^{-1})$
dP	Differential pressure	$(M\,L^{-1}\,T^{-2})$	(MPa)
dt	Time step	(T)	(s)
dx	Change in hydrate skin thickness	(L)	(m)
L	Distance from the brine-hydrate interface	(L)	(m)
L_c	Characteristic length	(L)	(m)
L_{filt}	Median filter diameter	(L)	(pixels)
m_m	Total mass of methane injected	(M)	(kg)
m_m^g	Mass of methane in the gaseous phase	(M)	(kg)
m_m^h	Mass of methane in the hydrate phase	(M)	(kg)
m_w	Total mass of brine removed	(M)	(kg)
m_{wi}	Initial mass of brine	(M)	(kg)
m_w^h	Mass of water in the hydrate phase	(M)	(kg)
m_w^l	Mass of brine in the liquid phase	(M)	(kg)
M_h	Hydrate molecular mass	$(M\,M^{-1})$	$(kg\,mol^{-1})$
M_m	Methane molecular mass	$(M\,M^{-1})$	$(kg\,mol^{-1})$
M_{salt}	Sodium chloride molecular mass	$(M\,M^{-1})$	$(kg\,mol^{-1})$
M_w	Water molecular mass	$(M\,M^{-1})$	$(kg\,mol^{-1})$
N	Hydration number for SI methane hydrate	(–)	(–)
P_{conf}	Confining pressure	$(M\,L^{-1}\,T^{-2})$	(MPa)
P_{eff}	Effective pressure	$(M\,L^{-1}\,T^{-2})$	(MPa)
P_{in}	Inlet pressure	$(M\,L^{-1}\,T^{-2})$	(MPa)
P_{out}	Outlet pressure	$(M\,L^{-1}\,T^{-2})$	(MPa)
P_{pore}	Pore pressure	$(M\,L^{-1}\,T^{-2})$	(MPa)
q_h	Hydrate formation rate	$(M\,T^{-1})$	$(mol\,s^{-1})$
q_{salt}	Salt flux	$(M\,T^{-1})$	$(mol\,s^{-1})$
r_{smpl}	Sample radius	(L)	(m)
S_g	Methane gas phase saturation	(–)	(–)
S_h	Solid hydrate phase saturation	(–)	(–)
S_{heq}	Three-phase equilibrium hydrate saturation	(–)	(–)
S_l	Liquid brine phase saturation	(–)	(–)
t	Time elapsed	(T)	(s)
T_{conf}	Confining temperature	(K)	(°C)
V^g	Volume of gaseous phase	(L^3)	(cm^3)

Table *(continued)*

Symbol	Name	Dimension	Unit
V^h	Volume of hydrate phase	(L^3)	(cm^3)
V_{aff}	Affected volume	(L^3)	(cm^3)
V_l	Volume of liquid brine removed	(L^3)	(cm^3)
V_m	Volume of methane gas injected	(L^3)	(cm^3)
V_{tot}	Total sample volume	(L^3)	(cm^3)
x	Hydrate skin thickness	(L)	(m)
x_{avg}	Average hydrate skin thickness	(L)	(m)
X^g	Volumetric gas phase ratio	(–)	(–)
X^h	Volumetric hydrate phase ratio	(–)	(–)
X_{conv}	Mass conversion ratio	(–)	(–)
X_{inj}	Volumetric injection ratio	(–)	(–)
α	Thermal diffusivity coefficient	($L^2\,T^{-1}$)	($m^2\,s^{-1}$)
β	Skempton compressibility coefficient	(–)	(–)
$\Delta\rho_b$	Bulk density change	($M\,L^{-3}$)	($g\,cm^{-3}$)
ϕ	Sample porosity	(–)	(–)
ϕ_{CT}	CT-derived sample porosity	(–)	(–)
ϕ_{grav}	Gravimetrically derived sample porosity	(–)	(–)
ρ_b^{avg}	Average bulk density of wet and dry sample	($M\,L^{-3}$)	($kg\,m^{-3}$)
ρ_b^{dry}	Bulk density of unsaturated sample	($M\,L^{-3}$)	($kg\,m^{-3}$)
ρ_b^{err}	Equivalent bulk density error	($M\,L^{-3}$)	($kg\,m^{-3}$)
ρ_b^{exp}	Experimental sample bulk density	($M\,L^{-3}$)	($kg\,m^{-3}$)
ρ_b^{wet}	Bulk density of saturated sample	($M\,L^{-3}$)	($kg\,m^{-3}$)
ρ_g	Gas phase density	($M\,L^{-3}$)	($kg\,m^{-3}$)
ρ_h	Solid hydrate density	($M\,L^{-3}$)	($kg\,m^{-3}$)
ρ_l	Liquid phase density	($M\,L^{-3}$)	($kg\,m^{-3}$)
ρ_s	Solid grain density	($M\,L^{-3}$)	($kg\,m^{-3}$)
τ	Generic heat conduction time scale	(T)	(s)

Acknowledgments

This work was supported by the U.S. Department of Energy under contracts DE-FE0010406, DE-FE0028967, and DE-FE0023919. Timothy Kneafsey was supported by the U.S. Department of Energy, Office of Fossil Energy, Office of Natural Gas and Petroleum Technology, through the National Energy Technology Laboratory, under award DE-AC02-05CH11231. All of the X-ray CT images and acquired data used in the figures are archived in the Digital Rocks Portal (www.digitalrocksportal.org) with the project name “Methane hydrate formation during gas injection into saturated sand.” All other experimental and analytical data referenced in this article are accessible through the presented figures, tables, and references. These data can also be requested by email from the corresponding author (meyerdw3@utexas.edu). We thank Peter Polito, Joshua O'Connell, and Skyler Dong for their assistance and advice in assembling the experimental apparatus and executing these experiments.

Appendix A: Computed Tomography Porosity Distribution

The bulk density of the saturated (ρ_b^{wet}) and unsaturated (ρ_b^{dry}) samples are functions of the sample porosity (ϕ) and the solid grain (ρ_s), liquid brine (ρ_l), and methane gas (ρ_g) densities (Table E1):

$$\rho_b^{wet} = ((1-\phi)\cdot\rho_s) + (\phi\cdot\rho_l) \quad \text{(A1)}$$

and

$$\rho_b^{dry} = ((1-\phi)\cdot\rho_s) + \left(\phi\cdot\rho_g\right). \quad \text{(A2)}$$

We calculate the change in bulk density between the saturated and unsaturated samples, assuming constant porosity, by subtracting equation A2 from A1 and solving for the porosity:

$$\phi = \frac{\rho_b^{wet} - \rho_b^{dry}}{\rho_l - \rho_g}. \quad \text{(A3)}$$

We solve for the CT-derived sample porosity (ϕ_{CT}) by assuming that the CT attenuation of a material is linearly proportional to its density and rewriting equation A3 in terms of the saturated (CT^{wet}) and unsaturated (CT^{dry}) CT attenuations and the attenuation contrast between pure brine and methane (CT^{l-g}):

$$\phi_{CT} = \frac{CT^{wet} - CT^{dry}}{CT^{l-g}}. \quad \text{(A4)}$$

Since the CT attenuations of pure brine and methane are unknown, we determine CT^{l-g} using the gravimetrically calculated bulk sample porosity (ϕ_{grav}; section (2.2)) and the average values for CT^{wet} and CT^{dry} across the sample:

$$CT^{l-g} = \frac{CT^{wet} - CT^{dry}}{\phi_{grav}}. \quad \text{(A5)}$$

Appendix B: CT Measurement Error Calibration

We quantify the CT measurement error (CT^{err}) by analyzing the attenuation data from the confining oil in 40 axial scans taken at experimental conditions and at the same position and scanning parameters. We use median filters with radii ranging from 1 to 50 pixels to replace the value at each individual pixel with the median value of the surrounding pixels. We then calculate the average standard deviation of the whole data set, equivalent to CT^{err}, for each median filter size (Figure B1).

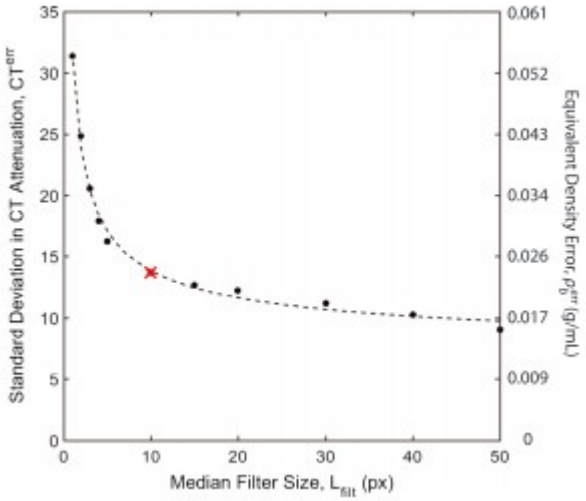

Figure B1

Standard deviation of the confining fluid computed tomography attenuation and equivalent density error at a range of median filter sizes (black dots). The dashed line indicates the power law fit of the data (equation B2). The red cross indicates the median filter size used during scan post processing.

We convert CT^{err} to an equivalent bulk density error (ρ_b^{err}; Figure B1) using the midpoint attenuation of the sample between the saturated and unsaturated scans (CT^{avg}; 1061 Houndfield units) and the midpoint bulk density of the wet and dry samples (ρ_b^{avg}; 1.84 g/cm^3):

$$\rho_b^{err} = \rho_b^{avg}\left(\frac{CT^{err}}{CT^{avg}}\right). \quad \text{(B1)}$$

The CT measurement error (Figure B1: black dots) decreases proportionally to the median filter size (L_{filt}) according to the following power law (Figure B1: black dashed line):

$$CT^{err} = \pm\left(\left(24.78 \cdot L_{filt}^{-0.55}\right) + 6.9\right). \quad \text{(B2)}$$

We use a 10-pixel median filter for our postprocessing as a balance between (1) standard-deviation reduction, (2) mean preservation, (3) data retention, and (4) conservation of actual heterogeneity, similar to previous studies (Pini et al., 2012; Seol & Kneafsey, 2009). With this filter, the CT^{err} ±13.4 Houndsfield units and the density threshold is ±0.024 g/cm^3 (Figure B1: red cross).

Appendix C: Mass Conversion and Volumetric Phase Ratios

We use mass balance to calculate the fraction of methane gas converted into hydrate and the amounts of hydrate and gas present in our sample over time. We calculate the mass conservation ratio (X_{conv}) from

$$X_{conv} = \frac{S_h V_{aff}}{V_m}\frac{M_m \rho_h}{\rho_g M_h} \text{ or} \quad \text{(C1)}$$

$$X_{conv} = 1 - \left(\frac{S_g V_{aff}}{V_m}\right). \quad \text{(C2)}$$

The phase densities and stoichiometric constants are shown in Table E1. We solve the volumetric injection ratio (X_{inj}) for the volume of methane injected ($V_m = X_{inj} V_l$) and substitute it into equations C1 and C2:

$$X_{conv} = \frac{S_h V_{aff}}{X_{inj} V_l} \frac{M_m \rho_h}{\rho_g M_h} \quad \text{(C3)}$$

and

$$X_{conv} = 1 - \left(\frac{S_g V_{aff}}{X_{inj} V_l}\right). \quad \text{(C4)}$$

We calculate the volumetric hydrate (X^h) and gas (X^g) phase ratios using

$$X^h = \frac{S_h V_{aff}}{V_l} \quad \text{(C5)}$$

and

$$X^g = \frac{S_g V_{aff}}{V_l}. \quad \text{(C6)}$$

We substitute equations C5 and C6 into equations C3 and C4, respectively, and solve for X^h and X^g:

$$X^h = X_{conv} X_{inj} \frac{\rho_g M_h}{M_m \rho_h} \quad \text{(C7)}$$

and

$$X^g = X_{inj}(1 - X_{conv}). \quad \text{(C8)}$$

We calculate the bulk gas (S_g) and hydrate (S_h) saturations assuming $V_l = 1$ mL and $V_{aff} = 100$ mL at a range of injection ratios (Appendix D). We then use equations C3, C7, and C8 to calculate X_{conv}, X^h, and X^g as a function of X_{inj}. This analysis indicates that, with no hydrate conversion ($X_{conv} = 0$), $X_{inj} = 1$, $X^g = 1$, and $X^h = 0$ and, with total hydrate conversion ($X_{conv} = 1$), $X_{inj} = 5.34$, $X^g = 0$, and $X^h = 4.93$.

Appendix D: Mass Balance-Derived Bulk Phase Saturations

We calculate the liquid brine (S_l), methane gas (S_g), and solid hydrate (S_h) bulk phase saturations within the affected volume using methane and brine mass balance and assuming the sum of the phases is equal to 1:

$$V_{aff} \rho_l S_l = V_{aff} \rho_l - V_l \rho_l - V_{aff} \frac{\rho_h N M_w}{M_h (1 - C_l)} S_h, \quad \text{(D1)}$$

$$V_{aff} \rho_g S_g = V_m \rho_g - V_{aff} \frac{\rho_h M_m}{M_h} S_h, \quad \text{(D2)}$$

and

$$1 = S_g + S_h + S_l. \quad \text{(D3)}$$

We measure the volumes of brine removed (V_l) and methane injected (V_m) by the change in volume on the syringe pumps. We determine affected volume (V_{aff}; section 2.5) using the CT scans. The initial brine salinity (C_i); assumed densities of the liquid (ρ_l), gas (ρ_g), and hydrate (ρ_h) phases; molecular masses of water (M_w), methane (M_m), and hydrate (M_h); and hydration number of Structure I methane hydrate (N) are shown in Table E1. We rearrange equations D1–D2 to isolate the unknowns:

$$V_{\text{aff}}\rho_l - V_l\rho_l = V_{\text{aff}}\rho_l S_l + V_{\text{aff}}\frac{\rho_h N M_w}{M_h(1-C_l)}S_h \quad \text{(D4)}$$

and

$$V_m\rho_g = V_{\text{aff}}\rho_g S_g + V_{\text{aff}}\frac{\rho_h M_m}{M_h}S_h. \quad \text{(D5)}$$

We combine and simplify equations D4 and D5 to remove S_h:

$$\frac{\rho_h\rho_l M_m}{M_h}(V_{\text{aff}} - V_l) - \frac{\rho_h\rho_g N M_w}{M_h(1-C_l)}V_m = \frac{\rho_h\rho_l M_m}{M_h}V_{\text{aff}}S_l - \frac{\rho_h\rho_g N M_w}{M_h(1-C_l)}V_{\text{aff}}S_g. \quad \text{(D6)}$$

We combine and simplify equations D3 and D5 to remove S_h:

$$\frac{\rho_h M_m}{M_h}V_{\text{aff}} - \rho_g V_m = \left(\frac{\rho_h M_m}{M_h}V_{\text{aff}} - \rho_g V_{\text{aff}}\right)S_g + \frac{\rho_h M_m}{M_h}V_{\text{aff}}S_l. \quad \text{(D7)}$$

We combine equations D6 and D7 to remove S_l and solve for S_g:

$$S_g = \frac{\frac{\rho_h}{M_h}\left(\frac{\rho_g M_w N V_m}{(1-C_l)} + \rho_l M_m V_l\right) - \rho_g\rho_l V_m}{V_{\text{aff}}\left(\frac{\rho_h}{M_h}\left(\frac{\rho_g M_w N}{(1-C_l)} + \rho_l M_m\right) - \rho_g\rho_l\right)}. \quad \text{(D8)}$$

We solve equation D7 for S_l and use equation D8 to calculate S_g within equation D9:

$$S_l = 1 - S_g + \frac{\rho_g M_h}{M_m\rho_h}\left(S_g - \frac{V_m}{V_{\text{aff}}}\right). \quad \text{(D9)}$$

We then solve equation D3 for the bulk hydrate saturation:

$$S_h = 1 - (S_g + S_l). \quad \text{(D10)}$$

Appendix E: Hydrate-Driven Salt Flux and Salt Concentration within a Finite Domain

E1. Hydrate Skin Growth

We derive an analytical solution for the thickness of the hydrate skin (x) over time (t) using a simple, one-dimensional model for methane diffusion across the hydrate skin. We assume the following: (1) Methane transport occurs by diffusion through the solid hydrate; (2) the methane concentration at the gas-hydrate interface equals the methane gas solubility in water (C_m^g); (3) the methane concentration at the brine-hydrate interface equals the hydrate

solubility in water (C_m^h); and (4) the diffusion rate can be approximated by a linear methane concentration profile across the hydrate. All the methane diffused through the hydrate forms additional hydrate, such that

$$D_m \frac{\left(C_m^g - C_m^h\right)}{x} dt = \frac{\rho_h}{M_h} dx. \quad \text{(E1)}$$

Equation E1 is integrated to solve for the hydrate skin thickness (x):

$$x = \sqrt{\frac{2D_m M_h \left(C_m^g - C_m^h\right)}{\rho_h}} \sqrt{t}. \quad \text{(E2)}$$

Table E1
Model and Stoichiometric Parameters at Our Experimental Conditions

Symbol	Name	Value
C_i	Initial salinity (kg kg^{-1})	0.07
C_{eq}	Three-phase equilibrium salinity (kg kg^{-1})	0.2125
C_m^g	Solubility of methane in water (mol m^{-3})	146.07
C_m^h	Solubility of hydrate in water (mol m^{-3})	61.09
D_c	Diffusion coefficient of salt in water (m s^{-2})[a]	10^{-9}
D_m	Diffusion coefficient of methane through hydrate (m s^{-2})[b,c]	10^{-15}
M_h	Molecular mass of Structure I (SI) methane hydrate (g mol^{-1})	119.655
M_m	Molecular mass of methane (g mol^{-1})	16.04
M_{salt}	Sodium chloride molecular mass (kg mol^{-1})	0.0584
M_w	Molecular mass of water (g mol^{-1})	18.02
N	Hydration number for SI methane hydrate[d,e,f]	5.75
ρ_s	Solid grain density (kg m^{-3})	2,650
ρ_g	Methane gas density (kg m^{-3})	112
ρ_l	Liquid brine density (kg m^{-3})	1,063
ρ_h	Solid hydrate density (kg m^{-3})	912

[a]Davie and Buffett (2001). [b]Genov et al. (2004). [c]Kuhs et al. (2006). [d]Uchida et al. (1995). [e]Sloan and Fleyfel (1991). [f]Davidson et al. (1986).

E2. Hydrate Driven Salt Flux

We derive an analytical solution for the salt flux (q_{salt}) at the brine-hydrate interface due to additional hydrate formation at that boundary. As the hydrate skin thickness increases due to hydrate formation (equation E2), it excludes salt into the brine at the interface and elevates the local salinity. We evaluate q_{salt} using

$$q_{salt} = q_h \frac{N M_w C_i}{(1 - C_i) M_{salt}}. \quad \text{(E3)}$$

We assume the water converted into hydrate comes from the brine near the brine-hydrate interface and that the salinity of that brine is equal to the initial salinity (C_i). We calculate the rate of hydrate formation (q_h) using

$$q_h = \frac{dx}{dt} \frac{\rho_h}{M_h}, \quad \text{(E4)}$$

where dx/dt is the derivative of the hydrate thickness (equation E2) with respect to time:

$$\frac{dx}{dt} = \sqrt{\frac{D_m M_h \left(C_m^g - C_m^h\right)}{2\rho_h}} \frac{1}{\sqrt{t}}. \quad \text{(E5)}$$

We substitute equation E5 into equation E4 and get

$$q_h = \sqrt{\frac{D_m \rho_h \left(C_m^g - C_m^h\right)}{2M_h}} \frac{1}{\sqrt{t}}. \quad \text{(E6)}$$

We then substitute equation E6 into equation E3 to solve for the salt flux:

$$q_{\text{salt}} = \frac{NM_w C_i}{(1 - C_i) M_{\text{salt}}} \sqrt{\frac{D_m \rho_h \left(C_m^g - C_m^h\right)}{2M_h}} \frac{1}{\sqrt{t}}. \quad \text{(E7)}$$

E3. Salt Concentration Profile Over Time

We use the salt flux (q_{salt}; equation E7) as a salt source at the brine-hydrate interface and derive a solution for the salt concentration with distance from the hydrate boundary (x) and time (t). The salt concentration (C) in the brine domain starts at initial concentration (C_i):

$$C(t = 0) = C_i. \quad \text{(E8)}$$

The governing equation for the change in salt concentration is

$$\frac{\partial C}{\partial t} = D_c \frac{\partial^2 C}{\partial x^2}. \quad \text{(E9)}$$

We impose a no transport boundary at the far edge of the brine domain:

$$\left.\frac{\partial C}{\partial x}\right|_{x = L_c} = 0. \quad \text{(E10)}$$

The boundary condition at the brine-hydrate interface is

$$-D_c \left.\frac{\partial C}{\partial x}\right|_{x=0} = q_{\text{salt}}, \quad \text{(E11)}$$

We substitute C^* for C in equations E8–E11, where $C^* = C - C_i$, and apply a Laplace transform to yield

$$\frac{d^2 \bar{C}^*}{dL^2} - \bar{C}^* \frac{s}{D_c} = 0, \quad \text{(E12)}$$

$$\left.\frac{d\bar{C}^*}{dx}\right|_{x = L_c} = 0, \text{ and} \quad \text{(E13)}$$

$$\left.\frac{d\bar{C}^*}{dx}\right|_{x=0} = \frac{A\sqrt{\pi}}{\sqrt{s}}. \quad \text{(E14)}$$

s is the Laplace transform parameter with respect to time, and A is

$$A = -\frac{NM_w C_i}{D_c (1 - C_i) M_{\text{salt}}} \sqrt{\frac{D_m \rho_h \left(C_m^g - C_m^h\right)}{2M_h}}. \quad \text{(E15)}$$

We find the solution to equations E12–E14:

$$\overline{C^*} = \frac{A\sqrt{\pi D_c}}{s}\left[\sinh\left(\sqrt{\frac{s}{D_c}}x\right) + \frac{\cosh\left(\sqrt{\frac{s}{D_c}}x\right)}{\tanh\left(\sqrt{\frac{s}{D_c}}L\right)}\right]. \quad \text{(E16)}$$

We obtain the solution to the salt concentration in actual time domain by applying a numerical inverse Laplace transform to equation E16 (Hoog et al., 1982).

References

Boswell, R., & Collett, T. (2011). Current prospective on gas hydrate resources. *Energy & Environmental Science*, 4, 10.

Boswell, R., Collett, T. S., Frye, M., Shedd, W., McConnell, D. R., & Shelander, D. (2012). Subsurface gas hydrate in the northern Gulf of Mexico. *Marine and Petroleum Geology*, 34, 27. https://doi.org/10.1016/j.marpetgeo.2011.10.003

Boswell, R., Frye, M., Shelander, D., Shedd, W., McConnell, D. R., & Cook, A. (2012). Architecture of gas-hydrate-bearing sands from Walker Ridge 313, Green Canyon 955, and Alaminos Canyon 21: Northern Deepwater Gulf of Mexico. *Marine and Petroleum Geology*, 34(1), 134– 149. https://doi.org/10.1016/j.marpetgeo2011.08.010

Boswell, R., Shelander, D., Lee, M., Latham, T., Collett, T., Guerin, G., et al. (2009). Occurrence of gas hydrate in Oligocene Frio sand: Alaminos Canyon Block 818: Northern Gulf of Mexico. *Marine and Petroleum Geology*, 26(8), 1499– 1512. https://doi.org/10.1016/j.marpetgeo.2009.03.005

Brusseau, M. L., Peng, S., Schnaar, G., & Costanza-Robinson, M. S. (2006). Relationships among air-water interfacial area, capillary pressure, and water saturation for a sandy porous medium. *Water Resources Research*, 42, W03501. https://doi.org/10.1029/2005WR004058

Brusseau, M. L., Peng, S., Schnaar, G., & Murao, A. (2007). Measuring air-water interfacial areas with X-ray microtomography and interfacial partitioning tracer tests. *Environmental Science & Technology*, 41(6), 1956–1961. https://doi.org/10.1021/es061474m

Casey, B., Germaine, J. T., Flemings, P. B., Reece, J. S., Gao, B., & Betts, W. (2013). Liquid limit as a predictor of mudrock permeability. *Marine and Petroleum Geology*, 44, 256– 263. https://doi.org/10.1016/j.marpetgeo.2013.04.008

Collett, T. S., Lee, M. W., Zyrinova, M. V., Mrozewski, S. A., Guerin, G., Cook, A. E., & Goldberg, D. S. (2012). Gulf of Mexico gas hydrate joint industry project leg II logging-while-drilling data acquisition and analysis. *Marine and Petroleum Geology*, 34, 21.

Cook, A. E., & Malinverno, A. (2013). Short migration of methane into a gas hydrate-bearing sand layer at Walker Ridge, Gulf of Mexico. *Geochemistry, Geophysics, Geosystems*, 14, 283– 291. https://doi.org/10.1002/ggge.20040

Crutchley, G. J., Fraser, D. R. A., Pecher, I. A., Gorman, A. R., Maslen, G., & Henrys, S. A. (2015). Gas migration into gas hydrate-bearing sediments on the southern Hikurangi margin of New Zealand. *Journal of Geophysical Research: Solid Earth*, 120, 725– 743. https://doi.org/10.1002/2014JB011503

Darnell, K. N., & Flemings, P. B. (2015). Transient seafloor venting on continental slopes from warming-induced methane hydrate dissociation. *Geophysical Research Letters*, 42, 10,765– 10,772. https://doi.org/10.1002/2015GL067012

Dash, J. G., Rempel, A. W., & Wettlaufer, J. S. (2006). The physics of premelted ice and its geophysical consequences. *Reviews of Modern Physics*, 78(3), 695– 741. https://doi.org/10.1103/RevModPhys.78.695

Davidson, D. W., Handa, Y. P., Ratcliffe, C. I., Ripmeester, J. A., Tse, J. S., Dahn, J. R., et al. (1986). Crystallographic studies of clathrate hydrates. Part I. *Molecular Crystals and Liquid Crystals*, 141(1–2), 141– 149. https://doi.org/10.1080/00268948608080205

Davie, M. K., & Buffett, B. A. (2001). A numerical model for the formation of gas hydrate below the seafloor. *Journal of Geophysical Research*, 106(B1), 497– 514. https://doi.org/10.1029/2000JB900363

Davie, M. K., & Buffett, B. A. (2003). A steady state model for marine hydrate formation: Constraints on methane supply from pore water sulfate profiles. *Journal of Geophysical Research*, 108(B10), 2495. https://doi.org/10.1029/2002JB002300

Davies, S. R., Sloan, E. D., Sum, A. K., & Koh, C. A. (2010). In situ studies of the mass transfer mechanism across a methane hydrate film using high-resolution confocal Raman spectroscopy. *The Journal of Physical Chemistry C*, 114(2), 1173– 1180. https://doi.org/10.1021/jp909416y

Davis, S. N., & DeWiest, R. J. M. (1967). *Hydrogeology*. New York, NY: John Wiley and Sons. https://doi.org/10.1016/0006-291X(67)90292-6

England, W. A., Mackenzie, A. S., Mann, D. M., & Quigley, T. M. (1987). The movement and entrapment of petroleum fluids in the subsurface. *Journal of the Geological Society*, 144(2), 327– 347. https://doi.org/10.1144/gsjgs.144.2.0327

Frye, M., Shedd, W., & Boswell, R. (2012). Gas hydrate resource potential in the Terrebonne Basin, northern Gulf of Mexico. *Marine and Petroleum Geology*, 34(1), 150– 168. https://doi.org/10.1016/j.marpetgeo.2011.08.001

Fu, X., Cueto-Felgueroso, L., & Juanes, R. (2018). Nonequilibrium thermodynamics of hydrate growth on a gas-liquid interface. *Physical Review Letters*, 120(14), 144501. https://doi.org/10.1103/PhysRevLett.120.144501

Genov, G., Kuhs, W. F., Staykova, D. K., Goreshnik, E., & Salamatin, A. N. (2004). Experimental studies on the formation of porous gas hydrates. *American Mineralogist*, 89(8–9), 1228– 1239. https://doi.org/10.2138/am-2004-8-910

Germaine, J. T., & Germaine, A. V. (2009). *Geotechnical laboratory measurements for engineers*. Hoboken, NJ: John Wiley & Sons, Inc. https://doi.org/10.1002/9780470548790

Ginsburg, G. D., & Soloviev, V. A. (1997). Methane migration within the submarine gas-hydrate stability zone under deep-water conditions. *Marine Geology*, 137(1–2), 49– 57. https://doi.org/10.1016/S0025-3227(96)00078-3

Haeckel, M., Suess, E., Wallmann, K., & Rickert, D. (2004). Rising methane gas bubbles form massive hydrate layers at the seafloor. *Geochimica et Cosmochimica Acta*, 68(21), 4335– 4345. https://doi.org/10.1016/j.gca.2004.01.018

Hassanzadeh, H., Pooladi-Darvish, M., Elsharkawy, A. M., Keith, D. W., & Leonenko, Y. (2008). Predicting PVT data for CO2-brine mixtures for black-oil simulation of CO2 geological storage. *International Journal of Greenhouse Gas Control*, 2(1), 65– 77. https://doi.org/10.1016/S1750-5836(07)00010-2

Hesse, R., & Harrison, W. E. (1981). Gas hydrates (clathrates) causing pore-water freshening and oxygen isotope fractionation in deep-water sedimentary sections of terrigenous continental margins. *Earth and Planetary Science Letters*, 55(3), 453– 462. https://doi.org/10.1016/0012-821X(81)90172-2

Hoog, F. R. d., Knight, J. H., & Stokes, A. N. (1982). An improved method for numerical inversion of Laplace transforms. *SIAM Journal on Scientific and Statistical Computing*, 3(3), 357– 366. https://doi.org/10.1137/0903022

Huo, Z., Hester, K., Sloan, E. D., & Miller, K. T. (2003). Methane hydrate nonstoichiometry and phase diagram. *AICHE Journal*, 49(5), 1300– 1306. https://doi.org/10.1002/aic.690490521

Jin, Y., Konno, Y., & Nagao, J. (2012). Growth of methane clathrate hydrates in porous media. *Energy & Fuels*, 26(4), 2242– 2247. https://doi.org/10.1021/ef3001357

Katsuki, D., Ohmura, R., Ebinuma, T., & Narita, H. (2007). Methane hydrate crystal growth in a porous medium filled with methane-saturated liquid water. *Philosophical Magazine*, 87(7), 1057– 1069. https://doi.org/10.1080/14786430601021652

Kneafsey, T. J., Tomutsa, L., Moridis, G. J., Seol, Y., Freifeld, B. M., Taylor, C. E., & Gupta, A. (2007). Methane hydrate formation and dissociation in a partially saturated core-scale sand sample. *Journal of Petroleum Science and Engineering*, 56(1–3), 108– 126. https://doi.org/10.1016/j.petrol.2006.02.002

Kuhs, W. F., Genov, G., Goreshnik, E., Zeller, A., Techmer, K. S., & Bohrmann, G. (2004). The impact of porous microstructures of gas hydrates on their macroscopic properties. *International Society of Offshore and Polar Engineers*, 14, 305– 309.

Kuhs, W. F., Klapproth, A., Gotthardt, F., Techmer, K., & Heinrichs, T. (2000). The formation of meso- and macroporous gas hydrates. *Geophysical Research Letters*, 27(18), 2929– 2932. https://doi.org/10.1029/2000GL006112

Kuhs, W. F., Staykova, D. K., & Salamatin, A. N. (2006). Formation of methane hydrate from polydisperse ice powders. *The Journal of Physical Chemistry B*, 110(26), 13,283– 13,295. https://doi.org/10.1021/jp061060f

Kvenvolden, K. A., & McMenamin, M. A. (1980). Hydrates of natural gas; a review of their geologic occurrence. Report Rep. 825. https://doi.org/10.1126/science.210.4475.1241

Lambe, T. W. (1969). *Soil mechanics*. New York: John Wiley & Sons, Inc.

Liu, X., & Flemings, P. B. (2006). Passing gas through the hydrate stability zone at southern Hydrate Ridge, offshore Oregon. *Earth and Planetary Science Letters*, 241, 16.

Liu, X., & Flemings, P. B. (2007). Dynamic multiphase flow model of hydrate formation in marine sediments. *Journal of Geophysical Research*, 112, B03101. https://doi.org/10.1029/2005JB004227

Malinverno, A., & Goldberg, D. S. (2015). Testing short-range migration of microbial methane as a hydrate formation mechanism: Results from Andaman Sea and Kumano Basin drill sites and global implications. *Earth and Planetary Science Letters*, 422, 105– 114. https://doi.org/10.1016/j.epsl.2015.04.019

Moridis, G. J., Collett, T., Boswell, R., Kurihara, M., Reagan, M. T., Koh, C., & Sloan, E. D. (2009). Toward production from gas hydrates: current status, assessment of resources, and simulation-based evaluation of technology and potential. *SPE Reservoir Evaluation & Engineering*, 12, 745– 771. https://doi.org/10.2118/114163-PA

Natarajan, V., Bishnoi, P. R., & Kalogerakis, N. (1994). Induction phenomena in gas hydrate nucleation. *Chemical Engineering Science*, 49(13), 2075– 2087. https://doi.org/10.1016/0009-2509(94)E0026-M

Nole, M., Daigle, H., Cook, A. E., & Malinverno, A. (2016). Short-range, overpressure-driven methane migration in coarse-grained gas hydrate reservoirs. *Geophysical Research Letters*, 43, 9500– 9508. https://doi.org/10.1002/2016GL070096

Olsen, H. W. (1966). Darcy's law in saturated kaolinite. *Water Resources Research*, 2(2), 9.

Onur, E. M. (2014). Predicting the permeability of sandy soils from grain size distribution. Master of Science, Kent State University, Ohio.

Pini, R., Krevor, S. C. M., & Benson, S. M. (2012). Capillary pressure and heterogeneity for the CO2/water system in sandstone rocks at reservoir conditions. *Advances in Water Resources*, 38, 48– 59. https://doi.org/10.1016/j.advwatres.2011.12.007

Pitzer, K. S. (1991). Ion interaction approach: Theory and data correlation. In K. S. Pitzer (Ed.), *Activity coefficients in electrolyte solutions* (2nd ed., pp. 75– 153). Boca Raton, FL: CRC Press.

Priegnitz, M., Thaler, J., Spangenberg, E., Rücker, C., & Schicks, J. M. (2013). A cylindrical electrical resistivity tomography array for three-dimensional monitoring of hydrate formation and dissociation. *Review of Scientific Instruments*, 84(10), 104502. https://doi.org/10.1063/1.4825372

Reagan, M. T., & Moridis, G. J. (2008). Dynamic response of oceanic hydrate deposits to ocean temperature change. *Journal of Geophysical Research*, 113, C12023. https://doi.org/10.1029/2008JC004938

Reagan, M. T., & Moridis, G. J. (2009). Large-scale simulation of methane hydrate dissociation along the West Spitsbergen Margin. *Geophysical Research Letters*, 36, L23612. https://doi.org/10.1029/2009GL041332

Rees, E. V. L., Kneafsey, T., & Seol, Y. (2011). Methane hydrate distribution from prolonged and repeated formation in natural and compacted sand samples: X-ray CT observations. *Journal of Geological Research*, 2011, 1– 15. https://doi.org/10.1155/2011/791815

Rempel, A. W. (2011). A model for the diffusive growth of hydrate saturation anomalies in layered sediments. *Journal of Geophysical Research*, 116, B10105. https://doi.org/10.1029/2011JB008484

Rempel, A. W., & Buffett, B. A. (1997). Formation and accumulation of gas hydrate in porous media. *Journal of Geophysical Research*, 102(B5), 10,151– 10,164. https://doi.org/10.1029/97JB00392

Rempel, A. W., Wettlaufer, J. S., & Worster, M. G. (2004). Premelting dynamics in a continuum model of frost heave. *Journal of Fluid Mechanics*, 498, 227– 244. https://doi.org/10.1017/s0022112003006761

Riedel, M., Novosel, I., Spence, G. D., Hyndman, R. D., Chapman, R. N., Solem, R. C., & Lewis, T. (2006). Geophysical and geochemical signatures associated with gas hydrate-related venting in the northern Cascadia margin. *GSA Bulletin*, 118(1–2), 23– 38. https://doi.org/10.1130/b25720.1

Riestenberg, D., West, O., Lee, S., McCallum, S., & Phelps, T. J. (2003). Sediment surface effects on methane hydrate formation and dissociation. *Marine Geology*, 198(1–2), 181– 190. https://doi.org/10.1016/S0025-3227(03)00100-2

Schowalter, T. T. (1979). Mechanics of secondary hydrocarbon migration and entrapment. *AAPG Bulletin*, 63(5), 37.

Seol, Y., & Kneafsey, T. J. (2009). X-ray computed-tomography observations of water flow through anisotropic methane hydrate-bearing sand. *Journal of Petroleum Science and Engineering*, 66(3–4), 121– 132. https://doi.org/10.1016/j.petrol.2009.01.008

Skempton, A. W. (1954). The pore-pressure coefficients A and B. *Géotechnique*, 4(4), 143– 147. https://doi.org/10.1680/geot.1954.4.4.143

Skovborg, P., Ng, H. J., Rasmussen, P., & Mohn, U. (1993). Measurement of induction times for the formation of methane and ethane gas hydrates. *Chemical Engineering Science*, 48(3), 445– 453. https://doi.org/10.1016/0009-2509(93)80299-6

Sloan, E. D., & Fleyfel, F. (1991). A molecular mechanism for gas hydrate nucleation from ice. *AICHE Journal*, 37(9), 1281– 1292. https://doi.org/10.1002/aic.690370902

Sloan, E. D., & Koh, C. A. (2007). *Clathrate hydrates of natural gases* (3rd ed.). Boca Raton, FL: CRC Press. https://doi.org/10.1201/9781420008494

Spangenberg, E., Kulenkampff, J., Naumann, R., & Erzinger, J. (2005). Pore space hydrate formation in a glass bead sample from methane dissolved in water. *Geophysical Research Letters*, 32, L24301. https://doi.org/10.1029/2005GL024107

Taylor, C. J., Miller, K. T., Koh, C. A., & Sloan, E. D. (2007). Macroscopic investigation of hydrate film growth at the hydrocarbon/water interface. *Chemical Engineering Science*, 62(23), 6524– 6533. https://doi.org/10.1016/j.ces.2007.07.038

Torres, M. E., McManus, J., Hammond, D. E., de Angelis, M. A., Heeschen, K. U., Colbert, S. L., et al. (2002). Fluid and chemical fluxes in and out of sediments hosting methane hydrate deposits on Hydrate Ridge, OR, I: Hydrological provinces. *Earth and Planetary Science Letters*, 201(3-4), 525– 540. https://doi.org/10.1016/S0012-821X(02)00733-1

Torres, M. E., Wallmann, K., Tréhu, A. M., Bohrmann, G., Borowski, W. S., & Tomaru, H. (2004). Gas hydrate growth, methane transport, and chloride enrichment at the southern summit of Hydrate Ridge, Cascadia margin off Oregon. *Earth and Planetary Science Letters*, 226(1–2), 225– 241. https://doi.org/10.1016/j.epsl.2004.07.029

Tréhu, A. M., Flemings, P. B., Bangs, N. L., Chevallier, J., Gràcia, E., Johnson, J. E., et al. (2004). Feeding methane vents and gas hydrate deposits at south Hydrate Ridge. *Geophysical Research Letters*, 31, L23310. https://doi.org/10.1029/2004GL021286

Uchida, T., Takagi, A., Kawabata, J., Mae, S., & Hondoh, T. (1995). Raman spectroscopic analyses of the growth process of CO2 hydrates. *Energy*

Conversion and Management, 36(6-9), 547– 550. https://doi.org/10.1016/0196-8904(95)00064-K

Ussler, W., & Paull, C. K. (2001). Ion exclusion associated with marine gas hydrate deposits. In *Natural gas hydrates: Occurrence, distribution, and detection* (pp. 41– 51). Washington DC: American Geophysical Union.

West, T. R. (2010). *Geology applied to engineering*. Long Grove, IL: Waveland Press.

Xu, W., & Ruppel, C. (1999). Predicting the occurrence, distribution, and evolution of methane gas hydrate in porous marine sediments. *Journal of Geophysical Research*, 104(B3), 5081– 5095. https://doi.org/10.1029/1998JB900092

Yamamoto, K., Terao, Y., Fujii, T., Ikawa, T., Seki, M., Matsuzawa, M., & Kanno, T. (2014). Operational overview of the first offshore production test of methane hydrates in the eastern Nankai Trough. Presented at the Offshore Technology Conference, Houston, TX.

You, K., DiCarlo, D., & Flemings, P. B. (2015). Quantifying hydrate solidification front advancing using method of characteristics. *Journal of Geophysical Research: Solid Earth*, 120, 6681– 6697. https://doi.org/10.1002/2015JB011985

You, K., & Flemings, P. B. (2017). Methane hydrate formation in thick sand reservoirs: 1. Short-range methane diffusion. *Marine and Petroleum Geology*. https://doi.org/10.1016/j.marpetgeo.2017.10.011

You, K., Kneafsey, T. J., Flemings, P. B., Polito, P., & Bryant, S. L. (2015). Salinity-buffered methane hydrate formation and dissociation in gas-rich systems. *Journal of Geophysical Research: Solid Earth*, 120, 643– 661. https://doi.org/10.1002/2014JB011190